

# Static mesh adaptation for reliable Large Eddy Simulation of turbulent reacting flows

P. W. Agostinelli,<sup>1,2, a)</sup> B. Rochette,<sup>2</sup> D. Laera,<sup>2</sup> J. Dombard,<sup>2</sup> B. Cuenot,<sup>2</sup> and L. Gicquel<sup>2</sup>

<sup>1)</sup>*Safran Helicopter Engines, Avenue Joseph Szydlowski, 64510 Bordes, France*

<sup>2)</sup>*CERFACS, 42 Avenue Gaspard Coriolis, 31057 Toulouse, France*

(Dated: 25 January 2021)

The design challenge of reliable lean combustors needed to decrease pollutant emissions has clearly progressed with the common use of experiments as well as Large Eddy Simulation (LES) because of its ability to predict the interactions between turbulent flows, sprays, acoustics and flames. However, the accuracy of such numerical predictions depends very often on the user's experience to choose the most appropriate flow modeling and, more importantly, the proper spatial discretization for a given computational domain. The present work focuses on the last issue and proposes a static mesh refinement strategy based on flow physical quantities. To do so, a combination of sensors based on the dissipation and production of kinetic energy coupled to the flame-position probability is proposed to detect the regions of interest where flow physics happens and grid adaptation is recommended for good LES predictions. Thanks to such measures a local mesh resolution can be achieved in these zones improving the LES overall accuracy while, eventually, coarsening everywhere else in the domain to reduce the computational cost. The proposed mesh refinement strategy is detailed and validated on two reacting-flow problems: a fully premixed bluff-body stabilized flame, i.e. the VOLVO test case, and a partially premixed swirled flame, i.e. the PRECCINSTA burner, which is closer to industrial configurations. For both cases, comparisons of the results with experimental data underline the fact that the predictions of the flame stabilization, and hence the computed velocity and temperature fields, are strongly influenced by the mesh quality and significant improvement can be obtained by applying the proposed strategy.

## I. INTRODUCTION

Few decades ago, Large Eddy Simulation (LES) had demonstrated its capability in predicting complex flows at Reynolds numbers that could not be reached by Direct Numerical Simulation (DNS), opening the opportunity of improving the understanding of turbulence in simple geometries<sup>1</sup>. Nowadays, thanks to the progress in computer technology and the significant advances in flow modeling (e.g. SGS models<sup>2,3</sup>, near-wall models), LES has become a reference method also for simulating flow physics in complex geometries, including swirling reacting flows in combustors<sup>4-7</sup>. In the aeronautical sector, together with experiments, because of its ability to accurately predict the interactions between turbulence, acoustic, spray and flame, the LES approach has been widely used<sup>8,9</sup> to study unsteady combustion thermoacoustic instabilities<sup>10,11</sup>, lean blow-off<sup>12,13</sup>, extinctions<sup>14,15</sup> or even to address pollutant emissions<sup>16,17</sup>.

However, the accuracy of these predictions often relies on the user's experience in choosing the most appropriate flow modeling along with the proper spatial discretization for a given computational domain. Sensitivity of the solution to the mesh is in fact a well-known issue in Computational Fluid Dynamics (CFD) both for non-reactive<sup>18-20</sup> and reactive flows<sup>5,21</sup>. In the context of Reynolds Averaged Navier-Stokes (RANS) prediction independence of the mesh is often requested and homogenous mesh refinement is commonly applied but it is also found to be computationally expensive and, therefore, not often practical<sup>22</sup>.

To circumvent such a challenge, Adaptive Mesh Refinement (AMR) methods have been developed in an attempt to

locally adapt a mesh. Two different philosophies are at the basis of AMR: Static Mesh Refinement (SMR) and Dynamic Mesh Refinement (DMR). SMR is more suitable for quasi-steady problems. It relies on computed flow statistics (e.g. mean field, RMS etc.) from which it is possible to identify flow regions where refinement is of interest. In these zones, h-refinement methods are usually applied subdividing the cells of a given mesh isotropically or anisotropically<sup>23,24</sup> until an optimised grid is obtained. On the contrary, DMR is more appropriate for unsteady cases where flow statistics have no specific physical meaning because the flow is in full transition: i.e. it evolves drastically in space and time (e.g. in explosion). This second strategy relies on an 'on-the-fly' evaluation of the important flow regions so that the spatial discretization of the computational domain changes as the computation proceeds. The optimized mesh can be obtained using p-refinement so that the order of discretization is locally increased avoiding changes in mesh topology. An alternative is to use a r-refinement in which cells of a given mesh are redistributed within the computational domain, clustering them in the zones of interest<sup>25</sup>. All of these different AMR methods have been developed and successfully applied to RANS for both non reactive flows<sup>26,27</sup> or reactive cases<sup>28</sup>. Applications to LES are clearly more difficult and rare mainly due to the only recent maturity of such an unsteady turbulence modeling approach<sup>29</sup>.

For non-reactive turbulent flows, AMR for LES has been assessed on structured meshes making use for example of the multi-scale decomposition theory<sup>30</sup>. Following RANS, anisotropic mesh adaptation using an Hessian-based error indicator considering small scale energy has also been recently proposed with the idea of identifying the optimal spatial resolution by minimizing the solution sensitivity<sup>31</sup>. The main limitation of these applications is linked to the use of struc-

<sup>a)</sup>Electronic mail: agostinelli@cerfacs.fr

tured mesh which can hardly manage complex geometries, leaving the method to be applicable only to turbulent channel flows or to flows on backward-facing steps and only recently to swirling flows<sup>32</sup>. The simulation of complex geometries indeed require unstructured grids. In this context, a double criterion ensuring both correct discretization of the mean field and a sufficient LES quality to ensure enough explicit prediction of the turbulent scale motions<sup>33</sup> has recently been proposed for iso-thermal flows in a complex meso-combustor<sup>34</sup>. Swirling flow have also been investigated<sup>35</sup>. In this case, the adopted AMR strategy consisted in defining regions where a mesh refinement was to be applied making use of a sensor based on the dissipation rate of kinetic energy, achieving an improvement on the prediction of the pressure losses through the swirlers.

For reactive flows, a grid sensitivity analysis has been recently obtained in the DNS framework for a turbulent hydrogen jet flame using a structured grid<sup>36</sup>. However, and to the author's knowledge, AMR of reactive LES is quasi inexistent even though literature does not lack of works where the impact of the mesh on the accuracy of the numerical predictions is addressed. For example, the VOLVO academic test-bench<sup>37-39</sup>, in which a fully premixed flame is stabilized behind a bluff-body, has been shown to be strongly sensitive to numerics<sup>40</sup>, chemical mechanisms<sup>41</sup>, thermal radiation<sup>42</sup> and also mesh refinement level<sup>43</sup>, making this configuration very well suited for a first application of LES AMR methods. A first application going in this direction was proposed by Drennan *et al.*<sup>44</sup> with a structured grid. Following the experience with Hessian-based AMR methods in RANS, cells were added in regions of large flow shear and temperature gradients in an attempt to obtain a grid independent LES prediction. Complementarily, systematic analysis of the solution mesh sensitivity for turbulent reactive flows has been recently performed on the partially premixed swirled flame in the well-known PRECCINSTA test bench<sup>45</sup>. Bénard *et al.*<sup>46</sup> compared solutions obtained on different unstructured meshes with increasing homogeneous refinement levels, evidencing how the flame stabilisation and lift-off is impacted by the mesh quality. This last work however did not propose an AMR strategy to efficiently refine the mesh in the required regions.

This paper aims at filling this gap of knowledge by proposing a SMR methodology so as to allow to refine a mesh and increase the accuracy of LES prediction while reducing the solution sensitivity to the grid. The method is based on three physical quantities (or Quantity of Interest, QOI<sup>35</sup>) computed from mean flow data, namely the dissipation rate of resolved kinetic energy, the production rate of the resolved turbulent kinetic energy and the probability to find the flame in a certain region. Once these fields are evaluated, it is possible to define the Region of Interest (ROI) where important flow physics happens and where higher mesh refinement level is required. To do so, QOIs are obtained and time-averaged during the computation (i.e. according to the SMR approach). They are provided to the MMG3D library<sup>47</sup> that refines the mesh in the ROI thanks to a h-refinement method. A new computation is then carried out on the refined mesh and QOI are again averaged to re-apply the refinement procedure if needed, follow-

ing the idea of iterative refinement proposed by Daviller *et al.*<sup>35</sup>. This strategy is applied and validated on the two previously mentioned configurations: the VOLVO and PRECCINSTA test-rigs.

The article is organized as follows. Criteria and strategy for the mesh refinement are detailed in Sec. II. Results on the VOLVO test case are discussed in Sec. III followed by the PRECCINSTA flame in Sec. IV.

## II. CRITERIA FOR MESH REFINEMENT

The proposed mesh adaptation strategy relies on a static mesh refinement procedure which aims at generalizing the original contribution proposed by Daviller *et al.*<sup>35</sup> to complex turbulent reacting flows. The idea behind this procedure is that the criteria at the basis of the mesh refinement should represent the important physics of the problem<sup>48</sup>. This can be done by selecting certain Quantity of Interests (QOIs) which flag the flow regions where physics happens and potentially require mesh refinement. Once a proper QOI is selected, the SMR procedure is applied. Note that the approach is iterative: (1) LES prediction is produced on an arbitrary initial mesh to compute average fields for a given QOI. (2) Starting from the QOI field, a metric field is computed containing the information on the desired local mesh refinement (or coarsening). (3) LES is performed on the new mesh, resulting in a novel evaluation of the QOIs. Such steps can then be repeated until the LES accuracy is deemed satisfactory.

To tackle turbulent reactive flows and define proper QOI's, the retained strategy divides the complexity of the problem into two distinct parts: the aerodynamics and the flame. The justification of this choice is twofold. First, from a practical point of view, what typically happens in reactive computations is that preliminary validations are conducted on corresponding non-reactive cases, so that aerodynamics should be first correctly captured. Second, from a physical point of view, it is evident that if aerodynamics is not well predicted, the flame cannot be correctly predicted since flame stabilization and dynamics are primarily driven by aerodynamics.

### A. Aerodynamics criteria

To point out the physical mechanisms that generate pressure losses in swirlers, Daviller *et al.*<sup>35</sup> proposed to look at the conservation equation for kinetic energy  $E_c = 1/2\rho u_i u_i$  which for constant-density flows<sup>49</sup> reads:

$$\underbrace{\frac{\partial E_c}{\partial t}}_1 + \underbrace{\frac{\partial}{\partial x_j} (u_j P_t)}_2 = \underbrace{\frac{\partial (\tau_{ij} u_i)}{\partial x_j}}_3 + \underbrace{\tau_{ij} \frac{\partial u_i}{\partial x_j}}_4. \quad (1)$$

In Eq. (1) terms (1), (2), (3) and (4) correspond to the temporal variation of the kinetic energy, the mechanical energy flux (i.e. advection of total pressure  $P_t$ ), the viscous diffusion

and the viscous dissipation respectively. The viscous dissipation term (4)  $\Phi$  controls the losses of total pressure  $P_t$  and hence the swirler pressure losses:

$$\Phi = \tau_{ij} \frac{\partial u_i}{\partial x_j} = \frac{\mu}{2} \left( \frac{\partial u_i}{\partial x_j} + \frac{\partial u_j}{\partial x_i} \right)^2. \quad (2)$$

$\Phi$  plays also an important role in turbulence theory since it corresponds to the fluid friction irreversibilities and controls the dissipation rate of the small scales<sup>50</sup>. Indeed, if considering a steady flow subject to no external force, it is possible to integrate Eq. (1) over the computational domain to express the pressure losses directly as a function of the integral of the volumetric dissipation rate:

$$Q_v \Delta P_t = \int_{flow\ domain} \Phi \, dV \quad (3)$$

where the first term represents the product of the volume flow rate  $Q_v$  and the pressure loss between inlet and outlet sections  $\Delta P_t$ . From Eq. (3) it is evident that to correctly predict the pressure loss across a swirler, LES should properly capture the dissipation rate.  $\Phi$  could then be used to construct the first QOI. However, while the equations above are exact for DNS, LES only solves for filtered velocity  $\tilde{u}_i$ <sup>51,52</sup>. This results in two contributions when evaluating the total resolved kinetic energy transport equation namely the laminar viscosity  $\mu$  and the turbulent viscosity  $\mu_t$  which takes into account the SGS model. Following these considerations, Daviller *et al.* proposed the definition of the metric *LIKE* constructed starting from the adimensionalized time-average dissipation rate QOI field ( $\Phi^*$ ):

$$\bar{\Phi} = (\mu + \mu_t) \overline{\left( \frac{\partial \tilde{u}_i}{\partial x_j} + \frac{\partial \tilde{u}_j}{\partial x_i} \right)^2}, \quad (4)$$

$$\Phi^* = \left[ 1 - \left( \frac{\bar{\Phi} - \bar{\Phi}_{\min}}{\bar{\Phi}_{\max} - \bar{\Phi}_{\min}} \right)^\alpha \right], \quad \Phi^* \in [0 : 1], \quad (5)$$

$$\text{LIKE} = \Phi^*(1 - \varepsilon) + \varepsilon. \quad (6)$$

In Eq. (5)  $\alpha$  is a smoothing parameter while  $\varepsilon$  in Eq. (6) allows limiting the new cell volume ( $\Delta$ ) which is reduced up to  $\varepsilon\Delta$  if  $\bar{\Phi} = \bar{\Phi}_{\max}$ . This is fundamental to avoid drastically reducing the time-step in explicit compressible LES codes subject to CFL condition. Note also that this formulation does not take into account dilatation dissipation due to compressibility effects<sup>53</sup> but it can be considered as a first order approximation for compressible flows.

While the LIKE criterion has been showed to be well suited to improve flow pressure loss predictions (more details in Ref.<sup>35</sup>), in order to completely characterise a turbulent flow in LES including the turbulent activity, the adequate unsteady velocity field should also be properly captured. Recalling the Reynolds decomposition to differentiate mean velocity  $\bar{u}_i$  from its fluctuation  $u'_i$ , performing the Favre and time average of Eq. (1), it is possible to obtain a balance equation for

the mean specific kinetic energy  $K = \frac{1}{2}(\bar{u}_i)^2$  and the turbulent specific kinetic energy  $k = \frac{1}{2}(\overline{u'_i})^2$  for constant-density flows reads:

$$\frac{DK}{Dt} = \underbrace{\overline{u'_i u'_j} \frac{\partial \bar{u}_i}{\partial x_j}}_2 - \underbrace{\nu \frac{\partial \bar{u}_i}{\partial x_j} \frac{\partial \bar{u}_i}{\partial x_j}}_3 + \underbrace{\frac{\partial}{\partial x_i} \left[ \nu \frac{\partial K}{\partial x_i} - \frac{\bar{p}}{\rho} \bar{u}_i - \overline{u'_i u'_i u'_i} \right]}_4, \quad (7)$$

$$\frac{Dk}{Dt} = \underbrace{-\overline{u'_i u'_j} \frac{\partial \bar{u}_i}{\partial x_j}}_2 - \underbrace{\nu \frac{\partial u'_i}{\partial x_j} \frac{\partial u'_i}{\partial x_j}}_3 + \underbrace{\frac{\partial}{\partial x_i} \left[ -\frac{\bar{p}' u'_i}{\rho} + 2\nu \overline{u'_i s'_{ii}} - \frac{1}{2} \overline{u'_i u'_i u'_i} \right]}_4. \quad (8)$$

The terms (1) in Eqs. (7), (8) correspond to the temporal variation of mean specific kinetic energy  $K$  and turbulent specific kinetic energy  $k$ , respectively. Terms (4) relate to the flux of mechanical energy. These terms disappear in the integral formulation over the fluid domain if the flow is subject to no power of external viscous forces. Terms (3) are the dissipation of the mean kinetic energy ( $\Phi_m$ ) and of the turbulent kinetic energy ( $\Phi_t$ ), respectively, their sum being  $\Phi$ . Note that the contribution of  $\Phi_m$  and  $\Phi_t$  to the temporal evolution of mean and turbulent kinetic energies is always negative meaning that they drain energy from the fluid and they dissipate the mechanical energy into heat. With the exception of the sign, terms (2) in Eqs. (7), (8) are equal and refer to the production of turbulent kinetic energy ( $P_k$ ). The  $P_k$  contribution can be either positive or negative, meaning that it represents a transfer of energy from the mean kinetic energy to the turbulent one and vice-versa. Adding Eqs. (7), (8) the conservation equation for the total specific kinetic energy averaged in time is obtained  $\bar{K}_c = \frac{1}{2}(\overline{u_i})^2 = \frac{1}{2}(\bar{u}_i)^2 + \frac{1}{2}(\overline{u'_i})^2 = K + k$ . In such a case, terms (2) cancel each other and the dissipation of total kinetic energy (formulated in Eq. (4) for LES) used in the previously defined LIKE criterion (Eq. (6)) is retrieved. These considerations highlight a possible limitation on the use of LIKE to capture the full dynamics of a turbulent flow, i.e., while the evolution of the total kinetic energy is well captured by LIKE, the same cannot be said for its distribution between mean and turbulent kinetic energy. The dynamics of the flow is therefore not guaranteed unless the absolute level of  $\Phi$  is known which is not the case in LES due to modelling.

To address this issue, it is interesting to look at the three different fields  $\Phi_m$ ,  $\Phi_t$  and  $P_k$  in the filtered LES formulation. These can then be used as QOI to identify the flow regions where the variation of turbulent and mean kinetic energy is maximum. Note that density is taken into account to be coherent with Eq. (4).

$$\bar{\Phi}_m = \overline{(\mu + \mu_t) \frac{\partial \bar{u}_i}{\partial x_j} \frac{\partial \bar{u}_i}{\partial x_j}}, \quad (9)$$

$$\bar{P}_k = -\overline{\bar{\rho} u'_i u'_j \frac{\partial \bar{u}_i}{\partial x_j}}, \quad (10)$$

$$\bar{\Phi}_t = \overline{(\mu + \mu_t) \frac{\partial u'_i}{\partial x_j} \frac{\partial u'_i}{\partial x_j}}. \quad (11)$$

A constructed field  $\Phi_{m,t,p}$  is hereby proposed as a combination of these three QOI:

$$\Phi_{m,t,p} = \beta \underbrace{\frac{\overline{\Phi_m} - (\overline{\Phi_m})_{min}}{(\overline{\Phi_m})_{max} - (\overline{\Phi_m})_{min}}}_1 + \gamma \underbrace{\frac{|\overline{P_k}| + \overline{\Phi_t} - (|\overline{P_k}| + \overline{\Phi_t})_{min}}{(|\overline{P_k}| + \overline{\Phi_t})_{max} - (|\overline{P_k}| + \overline{\Phi_t})_{min}}}_2. \quad (12)$$

Term (1) in Eq. (12) corresponds to the non-dimensional dissipation rate of mean kinetic energy  $\overline{\Phi_m}$ , while the term (2) is the non-dimensional sum of the absolute production  $|\overline{P_k}|$  and the dissipation rate of turbulent kinetic energy  $\overline{\Phi_t}$ . While the first term looks for regions where variations of mean kinetic energy are more important, the second one underlines regions where variations in turbulent kinetic energy are large. To balance the two contributions, the coefficients  $\beta$  and  $\gamma$  are here introduced. To choose their values, after the first refinement iteration in which they can be equal to 1, it is possible to look at the convergence rate of the mean ( $\beta$ ) and the turbulent ( $\gamma$ ) kinetic energies in the flow field with respect to the previous refinement iteration. Once the field  $\Phi_{m,t,p}$  is defined, it is possible to limit its variation in  $[\varepsilon : 1]$  following the same procedure as in Eqs. (5), (6).

## B. Flame criterion

Flames are usually too thin to be fully-resolved in numerical simulations. A combustion model is thus usually used to overcome this limitation. While multiple models could be found in the literature (see Ref.<sup>54</sup> for an exhaustive review) this work will deal with the Thickened Flame model (TFLES) in which flames are artificially thickened to be resolved on the mesh, without modifying their flame speeds<sup>55-60</sup>. The thickening process is done by multiplying diffusion terms and dividing reaction rates by a local thickening factor  $F$ . In case of a turbulent flame, since a thickened reactive layer is less sensitive to turbulence, an efficiency function  $\Xi_\Delta$  is introduced to compensate for the corresponding reduction of flame surface<sup>56,57</sup>.

The value of the thickening factor  $F$  is chosen in order to guarantee  $n_F$  points (usually between 5-8 depending on the complexity of the chemical description<sup>41</sup>) in the flame thermal thickness ( $\delta_T$ ) and can be locally evaluated as:

$$F(\vec{x}, t) = \frac{n_F \Delta_x(\vec{x})}{\delta_T(\phi, T)}, \quad (13)$$

where  $\Delta_x$  is the characteristic mesh size. Note that the local applied thickening factor  $F$  varies both in space  $\vec{x}$  and time  $t$  since  $\Delta_x$  is usually not uniform and varies in space and the thermal flame thickness  $\delta_T$  depends mainly on the equivalence ratio  $\phi$  and on the temperature  $T$  of the fresh gases which can vary as well both in space and time.

Following these definitions, to build a proper flame refinement criterion two data are needed: the time-averaged flame position and the local mesh size. The first can be easily computed using a flame sensor  $S$ . This sensor is equal to unity in the region where the flame is present and is zero elsewhere. It is straightforward to understand that the time-averaged field  $\overline{S}$  represents the local probability of finding a flame.

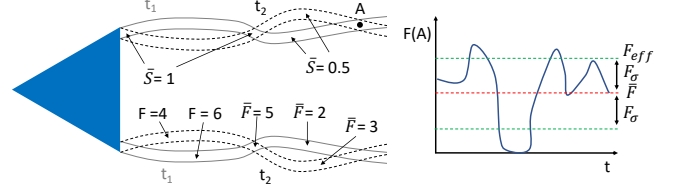


FIG. 1. Example of  $\overline{S}$  and  $\overline{F}$  fields. Flame has different position in the two instants  $t_1$  and  $t_2$  and different instantaneous  $F$ . It is evident how  $\overline{S}$  corresponds to the probability to locally find the flame and  $\overline{F}$  under-estimate the local thickening required.

In the regions detected by this sensor, a target flame resolution  $F_{target}$  can then be defined. By comparing this value with the time-averaged thickening  $\overline{F}$ , according to Eq. (13), the information on the characteristic mesh size is retrieved. However,  $\overline{F}$  may locally underestimate the thickening needed for the calculation. This is explained hereafter with the help of the schematic shown in Fig. 1: (1) combustion being an unsteady process, the flame may not always be locally present in a specific region. (2) Local variations of equivalence ratio (e.g. in partially premixed flames) may furthermore induce variations in flame thickness and hence in instantaneous locally applied  $F$ . To take into account these local variation of  $F$ , an effective thickening field  $F_{eff}$  can be reconstructed from the time-averaged field  $\overline{F}$  and its standard deviation  $F_\sigma$ :  $F_{eff} = \overline{F} + F_\sigma$ .<sup>61</sup>

Once the field  $F_{eff}$  is computed and a suitable  $F_{target}$  chosen, it is possible to build the Flame Effective Thickening (FET) metric as follows:

$$FET = \begin{cases} \frac{F_{target}}{F_{eff}} & \text{if } \overline{S} \geq S_{limit} \text{ and } F_{target} \leq F_{eff} \\ 1 & \text{elsewhere,} \end{cases} \quad (14)$$

where  $S_{limit}$  is a threshold value on the flame sensor. The refined mesh is then obtained by multiplying each cell characteristic size  $\Delta_x$  by the FET metric achieving the desired resolution (i.e. desired thickening  $F$ ) in the region where the probability to find the flame is higher or equal to  $S_{limit}$ . Using the FET metric, it is also straightforward to compute an *a priori* (i.e. before refinement) estimation of the required number of cells of the refined mesh ( $N_{refined}$ ) as a function of  $F_{target}$  and  $S_{limit}$ :

$$N_{refined} = \sum_i^{N_{coarse}} \left( \frac{\Delta_x \text{ refined}}{\Delta_x \text{ coarse}} \right)_i^3 = \sum_i^{N_{coarse}} \left( \frac{1}{FET} \right)_i^3. \quad (15)$$

Note also that this approach can be easily extended to cover other sub-grid combustion models. In fact, the flame sensor  $S$ , and hence the flame probability  $\overline{S}$ , can always be defined independently from the sub-grid combustion model used. For example, starting from the heat release rate field  $\dot{q}$  one can choose to set  $S = 1$  in the region where  $\dot{q}$  is larger than a certain threshold value. Equivalently an iso-C (i.e. progress variable) or iso-Z (i.e. mixture fraction) values can be introduced in place of  $\overline{S}$  (any combustion marker would work). In

this way the reactive ROI can be defined following the same procedure. The only difference stays in the refinement level which cannot be chosen on the base of the thickening factor  $F$  for other specific turbulent combustion models. However, it is straightforward to select the refinement level in order to have the desired mesh size with respect to the characteristic length of the problem, for example the thermal flame thickness  $\delta_T$ .

### C. Refinement procedure

The two previously defined QOI's for aerodynamics and flame are now combined following the two procedures schematized in Fig. 2 to either build an optimal mesh or optimize an existing one (to avoid waste of computational resources).

The procedure to optimize an existing mesh is straightforward: first LES is computed on the reference mesh to evaluate the QOI's  $\overline{\Phi}_m$ ,  $\overline{\Phi}_t$ ,  $\overline{P}_k$  and  $\overline{S}$ . Then it is possible to identify the ROI by defining limits on the QOI: for example  $\overline{\Phi}_{mlimit} = 0.01 * \overline{\Phi}_{mmax}$ ,  $\overline{\Phi}_{tlimit} = 0.01 * \overline{\Phi}_{tmax}$  and  $\overline{P}_{klimit} = 0.01 * \overline{P}_{kmax}$  to identify the ROI where most of mean kinetic energy dissipation and production or dissipation of turbulent kinetic energy happen while a  $\overline{S}_{limit} = 0.01$  defines the ROI where there is a large probability to find the flame. The ROI can be defined as the union of these regions, as follows,

$$ROI = \left( \overline{\Phi}_m \geq \overline{\Phi}_{mlimit} \right) \cup \left( \overline{\Phi}_t \geq \overline{\Phi}_{tlimit} \right) \cup \left( |\overline{P}_k| \geq |\overline{P}_k|_{limit} \right) \cup \left( \overline{S} \geq \overline{S}_{limit} \right). \quad (16)$$

A uniform metric  $D$  (larger than 1) can be then defined in the rest of the domain to derefine the mesh. LES is performed on the new mesh reiterating the described procedure if needed.

The building of an optimal mesh starting from an arbitrary initial mesh follows the initial step of computing the QOI's. At this point, due to the possible additional difficulty of a totally wrong initial solution, a check on the accuracy of the aerodynamics prediction is needed. If accuracy is not satisfactory, based on an analysis of the fields  $\overline{\Phi}_m$ ,  $\overline{\Phi}_t$ ,  $\overline{P}_k$  it is possible to decide to use the LIKE metric with proper  $\alpha$  parameter or  $\Phi_{m,t,p}^*$  metric if  $\overline{\Phi}_t$ ,  $\overline{P}_k$  happen in different regions of the domain. The refinement step brings to a new mesh on which LES can be computed and accuracy of the aerodynamic field checked until it becomes satisfactory. At this point, if the flame prediction is not accurate, the FET metric can be evaluated and used to refine the mesh in the flame region. The iterative refinement procedure finally leads to an optimum mesh with the desired solution accuracy. In the following both proposed strategies are first applied and validated on the academic VOLVO test case (Sec. III). The methodology is then applied to the PRECCINSTA rig (Sec. IV) showing that the method can be successfully applied to more complex configurations.

## III. A FULLY PREMIXED BLUFF-BODY STABILIZED FLAME: THE VOLVO TEST CASE

Well-known as a benchmark for turbulent reacting simulations<sup>62-64</sup>, the VOLVO combustor<sup>37-39</sup> consists in a 3D propane-air turbulent premixed flame burning in a straight rectangular cross-section channel (0.12 m  $\times$  0.24 m). A bluff-body flame-holder is used to stabilize the flame. Fresh gas conditions are  $T = 288 K$  and  $P = 101325 Pa$ . The computational domain shown in Fig. 3 has the exact longitudinal and transverse dimensions as the original burner. LES are performed using the AVBP solver developed by CERFACS.<sup>65</sup> It solves the fully compressible Navier-Stokes multispecies equations on unstructured grids. The flow is integrated using the fully compressible explicit Lax-Wendroff (LW) convection scheme<sup>66</sup> (second order in time and space). Inlet and outlet boundary conditions are treated with Navier-Stokes Characteristic Boundary Conditions (NSCBC)<sup>51</sup>. These two boundary conditions are modeled as non-reflecting sections to avoid exciting a particular acoustic mode. At the inlet, gaseous propane is premixed with air at an equivalence ratio equal to 0.65 and injected at an inlet bulk velocity  $U_0 = 17.3 m/s$ . Turbulence is injected at the inlet using the method of Guezennec *et al.*<sup>67</sup> to recover the turbulence intensity measurements<sup>37</sup>. As the wall temperature is not provided in the experiments<sup>37</sup>, the walls are modeled as adiabatic no-slip walls. The TFLES model with the Charlette model<sup>57</sup> and a coefficient  $\beta_{Ch} = 0.5$  is used.

### A. Results and discussion

Validation of the proposed methodology is hereafter detailed for the optimization of an existing mesh (Sec. III A 1) and afterward to look for an optimal mesh (Sec. III A 2).

#### 1. Optimizing an existing mesh

The previously proposed strategy (Fig. 2) is at first assessed. To do so, the previous calculations of this flame using the same solver performed by Rochette *et al.*<sup>41</sup> is used as a reference. Figure 4 reports the averaged field of heat release rate  $\overline{q}$  and the thickening factor  $\overline{F}$  fields predicted by Rochette *et al.*<sup>41</sup> superimposed on the computational grid. With this grid the flame is anchored to the flame-holder between the recirculation zone and the high sheared fresh gas region. It is wrinkled by the eddies generated by the bluff-body and burns until the end of the combustion chamber. The grid consists of 68 million tetrahedral elements for which the mesh has been manually refined in shear and combustion regions achieving a  $\Delta_x = 500 \mu m$  just downstream of the flame-holder. This results in a near wall region of the flame holder dimensionless wall distances of  $y^+ = 25$ , versus  $y^+ = 80$  near the combustor walls. It is possible to notice that the mesh exhibits clusters of cells where no important physics occurs. Following the strategy, the ROI are identified using the previously described QOIs.

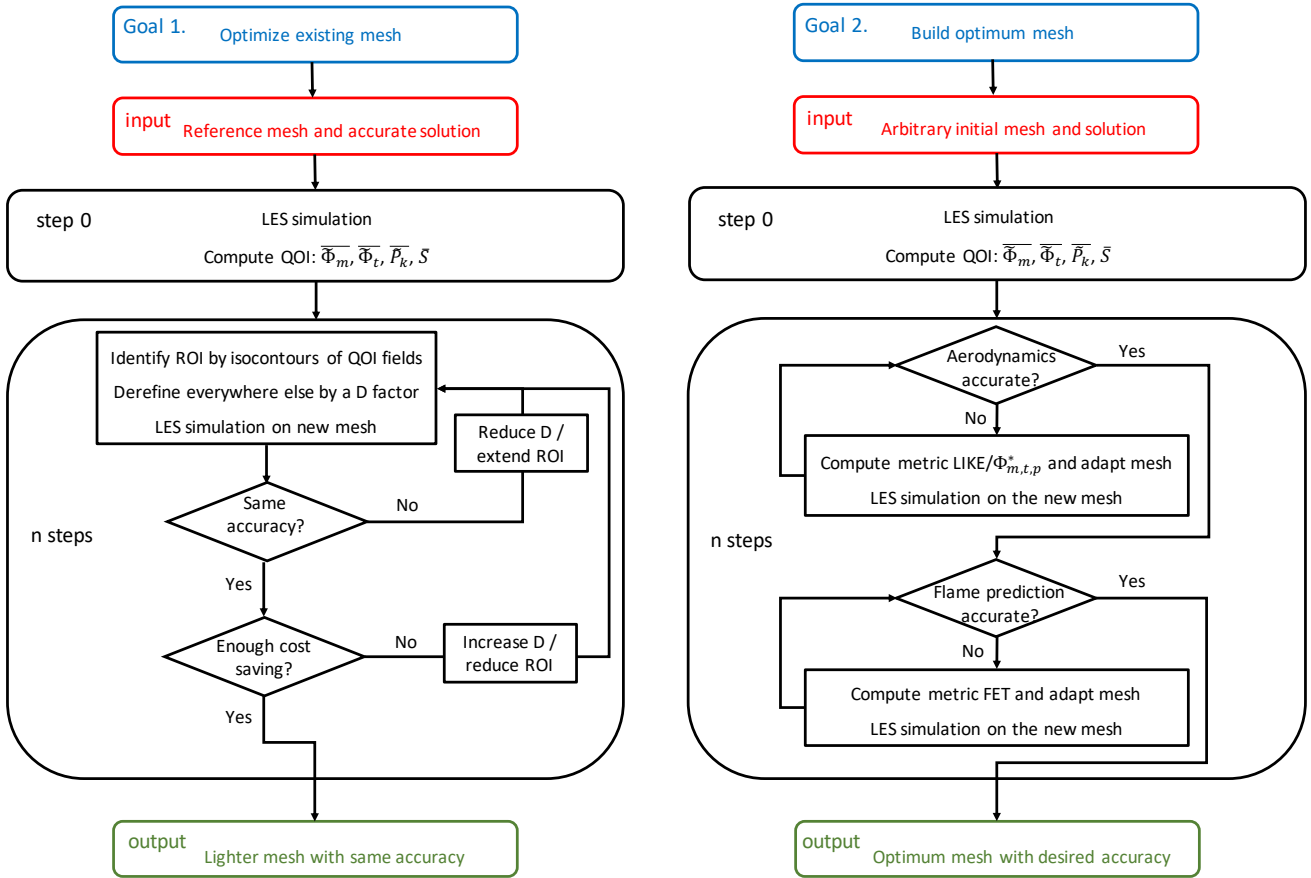


FIG. 2. Scheme of the two mesh adaptation procedures: optimization of existing reference mesh and building of optimal mesh from initial arbitrary one.

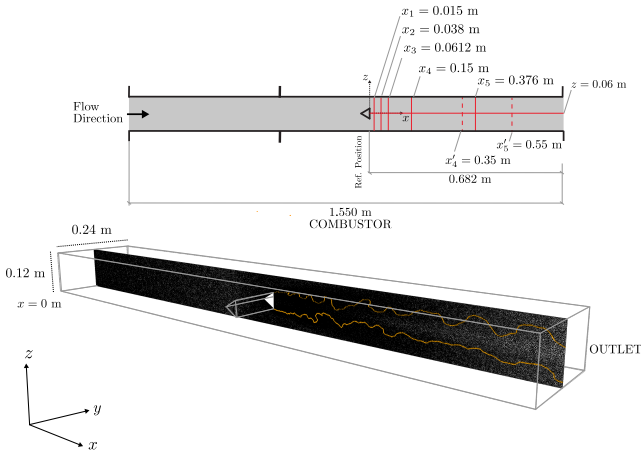


FIG. 3. Overview of the computational domain. The flame is represented through an iso-contour of progress variable  $c = 0.5$  (orange line). Measurements were made on seven longitudinal ( $x_1, x_2, x_3, x_4, x'_4, x'_5$  and  $x_5$ ) and one ( $z$ ) transverse locations.

Regions of large mean and turbulent kinetic energy dissipation rate are respectively identified by  $\bar{\Phi}$  (Eq. (4)) and  $\bar{\Phi}_m$

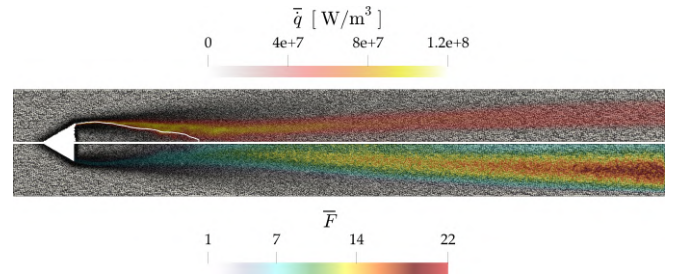


FIG. 4. Overview of the reference mesh (68M) used by Rochette *et al.*<sup>41</sup>. The flame is represented through an averaged field of heat release rate  $\bar{q}$ . The averaged thickening factor field  $\bar{F}$  is also shown. The white iso-contour delimits the recirculation zone ( $U_x = 0$  m/s).

(Eq. (9)) as presented in Fig. 5. The  $\bar{\Phi}$  field activates in shear regions just downstream of the flame-holder as well as at the boundary of the recirculation zone and in the boundary-layer nearby the walls. The  $\bar{\Phi}_m$  field well detects the dissipation of mean kinetic energy that happens in the wall boundary-layers and in the shear region downstream of the bluff-body. The magnitude of these two fields is comparable, confirming that most of the kinetic energy dissipation acts on the mean form in the shear-region downstream the bluff-body. The gray and

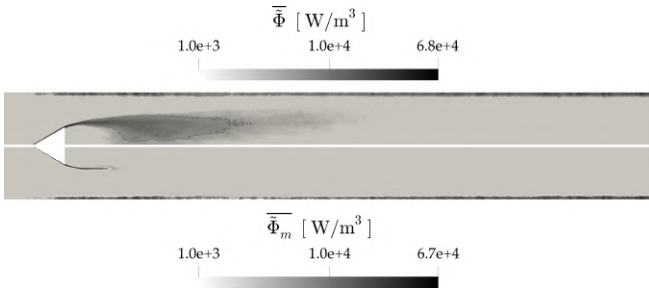


FIG. 5. QOI fields of  $\bar{\Phi}$  and  $\bar{\Phi}_m$  for case 68M. The grey and the white iso-contour delimit the ROI where most of the kinetic energy dissipation happen with the values of  $\bar{\Phi} = 0.01 \bar{\Phi}_{max}$  and  $\bar{\Phi}_m = 0.01 \bar{\Phi}_{mmax}$  respectively. Note that log scale is used.

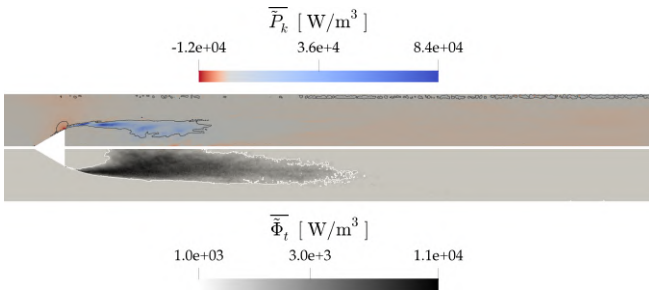


FIG. 6. QOI fields of  $\bar{P}_k$  and  $\bar{\Phi}_t$  for case 68M. The gray and the white iso-contours correspond to  $|\bar{P}_k| = 0.01 |\bar{P}_k|_{max}$  and  $\bar{\Phi}_t = 0.01 \bar{\Phi}_{tmax}$  and identify the regions where large production and dissipation rates of turbulent kinetic energy happen respectively. Note that log scale is used only for  $\bar{\Phi}_t$  field.

the white iso-contours correspond to  $\bar{\Phi} = 0.01 \bar{\Phi}_{max}$  and  $\bar{\Phi}_m = 0.01 \bar{\Phi}_{mmax}$  and identify the ROI where most of the dissipation happens.

The QOI fields of  $\bar{P}_k$  (Eq. 10) and  $\bar{\Phi}_t$  (Eq. 11) are compared in Fig. 6. The gray and the white iso-contours correspond to  $|\bar{P}_k| = 0.01 |\bar{P}_k|_{max}$  and  $\bar{\Phi}_t = 0.01 \bar{\Phi}_{tmax}$  and identify the regions where large production and dissipation rates of turbulent kinetic energy happen, respectively. Production is positive in the region upstream the bluff-body's corner where the flow axially accelerates and turbulent kinetic energy is converted into mean kinetic energy, reducing the turbulence activity in the flame region. In the downstream shear-layer production is negative, indicating that turbulence and eddies are produced by the bluff-body. In the latter,  $\bar{\Phi}_t$  is also activated and its intensity reduces moving downstream as turbulence is no more produced and dissipated. Analysis of the QOI magnitudes suggest that  $\bar{\Phi}_t$  is much lower than  $\bar{P}_k$  and  $\bar{\Phi}_m$ . Therefore, when it is added to  $\bar{\Phi}_m$ , the resulting  $\bar{\Phi}$  field is very similar to the  $\bar{\Phi}_m$ . This explains why, when an  $\alpha$  value of 1 in the LIKE criterion is imposed, the mesh is refined just in the region where  $\bar{\Phi}_m$  is present. On the contrary, if a large  $\alpha$  value is used, more effort is concentrated to smaller  $\bar{\Phi}$  values which correspond to regions where  $\bar{\Phi}_t$  is present. Note also that regions of large negative  $\bar{P}_k$  and large  $\bar{\Phi}_t$  largely corre-

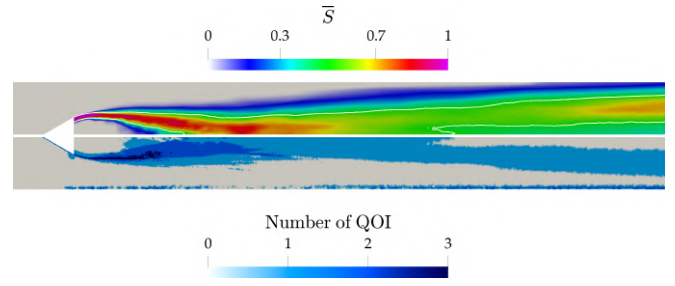


FIG. 7. QOI field of  $\bar{S}$  for case 68M and number of matching criteria delimiting a ROI. The white iso-contour correspond to  $\bar{S} = 0.5$

spond (i.e. shear-layer downstream the bluff-body and middle region) since when turbulence is produced its dissipation also increases. On one side, the analysis of these fields suggest that, for the present case, taking into consideration a  $\bar{\Phi} = 0.01 \bar{\Phi}_{max}$  defines a sufficiently large ROI that includes regions where large dissipation of mean and turbulent kinetic energy happen ( $\bar{\Phi}_m$  and  $\bar{\Phi}_t$ ). On the other side, while the region where  $\bar{P}_k$  is negative is well captured by the  $\bar{\Phi} = 0.01 \bar{\Phi}_{max}$  iso-contour, in the region where production is negative no dissipation happens and it must be taken into account by defining a ROI delimited by the  $|\bar{P}_k| = 0.01 |\bar{P}_k|_{max}$  for example. In the present case the union of the regions delimited by  $\bar{\Phi}$  and  $|\bar{P}_k|$  are able to identify a ROI where most of the aerodynamics activity happens.

For the reactive part, the time-averaged flame sensor  $\bar{S}$  is shown in Fig 7. The bluff-body region exhibits a  $\bar{S}$  equal to unity suggesting an attached flame. Moving downstream,  $\bar{S}$  is more spread indicating oscillations of the reactive layer due to interaction with the eddies generated by the bluff-body. A value of  $\bar{S} = 0.5$  is sufficient in this case to flag the ROI (i.e., where the probability to find the flame is higher than 50%). Finally, the bottom part of Fig. 7 shows the number of QOI's which are locally activated simultaneously. The zone where no QOI is active will be coarsened (by an iso-factor D of 2), whereas the remaining mesh will be untouched. Observing the entire ROI, the only zone where all three QOIs are activated locates in the shear-layer region after the bluff body where large aerodynamics activity and flame are both present. Otherwise only one QOI seems at once underlining the importance of using all three quantities of interests to capture all the physics of the problem.

The resulting optimised mesh shown in Fig. 8 consists of 45M cells, i.e., 33% lighter with respect to the reference one<sup>68</sup>. As expected the mesh is finer in the shear and flame regions and coarser in fresh and burnt gas zones.

The time-averaged heat release rate  $\bar{q}$  and thickening factor field  $\bar{F}$  for the optimized mesh case (45M) can be compared to the reference mesh of Fig. 4. The heat release rate fields are very similar, while looking at  $\bar{F}$ , it is possible to observe an increase of the thickening factor along the axial direction with respect to the reference mesh. This behaviour is linked to the increasing cell sizes. Such maximum thickening values are not pathological for the simulation, but obviously the

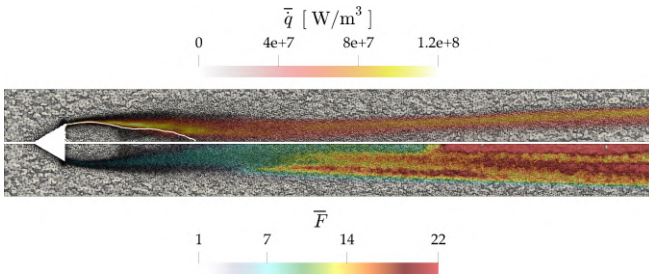


FIG. 8. Overview of the 45M optimized mesh obtained by coarsening regions where no important physics occurs. The flame is represented through an averaged field of heat release rate  $\bar{q}$ . Time-averaged thickening factor field  $\bar{F}$  is also shown. The white iso-contour delimits the recirculation zone ( $U_x = 0$  m/s).

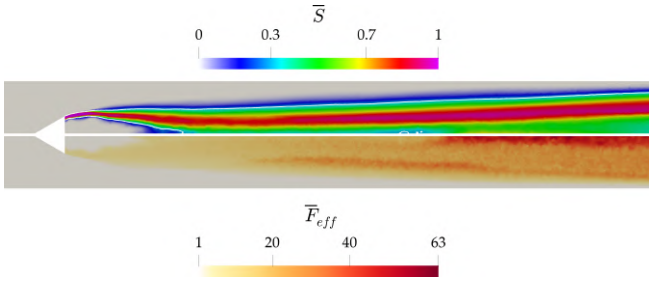


FIG. 9. QOI fields of flame probability  $\bar{S}$  and the effective thickening  $\bar{F}_{eff}$  for case 45M. The white iso-contour correspond to  $\bar{S} = 0.3$

bigger are the cell sizes, the lower the accuracy of the LES in predicting flame-turbulence interaction.

A second possible exercise could be to further refine this 45M elements mesh up to the same cost as the one of the reference mesh (i.e.,  $\simeq 68$ M), to verify if better results can be obtained. Since the aerodynamic field is now well-captured, the FET criterion is hereby used. The flame probability  $\bar{S}$  and the effective thickening field  $\bar{F}_{eff}$  for the optimized 45M mesh are presented in Fig. 9. The ROI where the probability to find the flame is higher than 30% can then be easily flagged by the line where  $\bar{S}=0.3$  (white iso-contour), top part of Fig. 9. The field  $\bar{F}_{eff}$  can then be used to build the FET metric as explained in Sec. II B. However, in the present application, the idea is to improve the reference mesh without overcoming a fixed computational cost. To do so,  $F_{target}$  is fixed following Eq. (15) in order to have very similar number of cells as in the reference mesh. In that case, the *a priori* evaluation of cells number leads to  $F_{target} \approx 40$  and to a refined mesh with 67M of cells which is comparable to the reference mesh. The resulting mesh (67M) in shown in Fig. 10. It has the same cost as the reference mesh but with a better resolution in the ROI. As expected the mesh is finer at the end of the burner in combustion regions.

The time-averaged heat release rate  $\bar{q}$  and thickening factor field  $\bar{F}$  for the refined mesh case (67M) are superimposed to the grid in Fig. 10. The averaged flame and the recirculation zone (white iso-contour) downstream the bluff-body are very similar to the 45M and 68M cases. However, it is evident that  $\bar{F}$  is much more homogeneous, especially in the region far

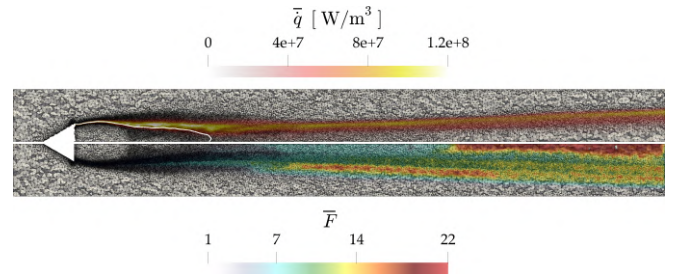


FIG. 10. Overview of the 67M optimized mesh obtained by refining in high thickening regions using the FET criterion. The flame is represented through a time-averaged field of heat release rate  $\bar{q}$ . The time-averaged thickening factor field  $\bar{F}$  is also shown. The white iso-contour delimits the recirculation zone ( $U_x = 0$  m/s).

downstream as expected and the instantaneous applied thickening  $F$  is statistically always lower than  $F_{target}$ .

A comparison of the three aerodynamic predicted fields and the experiments is finally presented to further validate the refinement procedure in Fig. 11. The axial profiles of the mean axial velocity component are reported in Fig. 11(a). It is evident how the reference mesh and the optimized 45M mesh give very similar results, confirming that the ROI where important physics happen are well identified by the proposed procedure. The 67M mesh instead shows improved results in the prediction of the recirculation zone and also in the acceleration of the burnt gases, which is a direct result of the increased resolution in the last part of the combustion chamber. The mean normalized axial velocity component is well captured in all cases, as showed by the transverse profiles at different measurement planes in Fig. 11(b), confirming that the optimized 45M mesh does not worsen the LES prediction of the reference mesh. Same conclusions can be deduced by looking at transverse profiles of normalized RMS of the axial and transverse velocity fluctuations from  $x_1$  to  $x_5$  shown in Fig. 11(c-d), respectively. The optimized 45M mesh gives the same solution accuracy as the reference case and the refined mesh (67M) shows closer results to the experimental data, for example in the prediction of low turbulence activity (low  $U_{rms}$  values) far from the axis.

## 2. Building an optimum mesh

The second refinement strategy proposed in Fig. 2 is now discussed. It consists in building an optimum mesh from an arbitrarily (coarse) one which in this case is the 10M mesh shown in Fig. 12 together with the predicted time-averaged heat release rate  $\bar{q}$  and thickening field  $\bar{F}$ . Due to a poor mesh resolution, the flame shape is totally wrong compared to the reference case: the flame is short and burns inside of the wake of the flame-holder and the recirculation zone (white iso-contour) is too long. The objective is thus to converge to a correct solution starting from a wrong one through the mesh refinement strategy.

Following the mesh refinement procedure, all QOI's are computed on the coarse mesh. Total dissipation rate of ki-

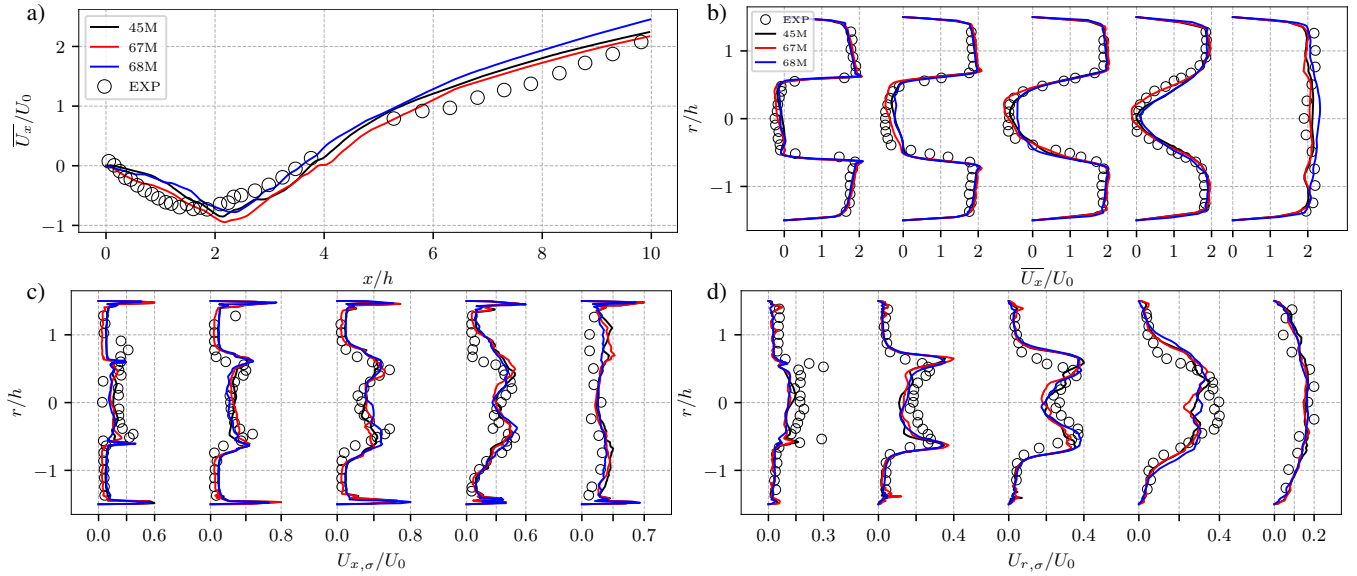


FIG. 11. Comparison between experimental velocity profiles and LES for the 45M, 67M and 68M (reference) cases. Mean axial velocity evolution along the central axis (a). Transverse profiles at measurement planes  $x_1$ - $x_5$  of the mean normalized axial velocity (b), the normalized RMS axial velocity component (c) and the normalized RMS transverse velocity component (d).

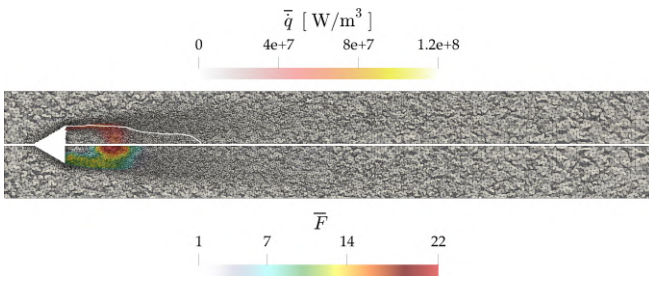


FIG. 12. Overview of the initial 10M coarse mesh obtained by coarsening by a factor of two everywhere in the domain the reference mesh. The flame is represented through an averaged field of heat release rate  $\overline{q}$ . Thickening factor field  $\overline{F}$  is also shown. The white iso-contour delimits the recirculation zone ( $U_x = 0$  m/s).

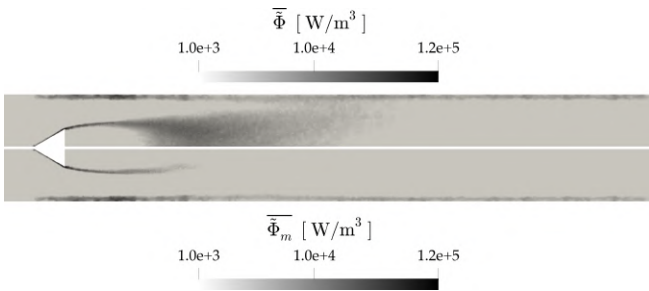


FIG. 13. QOI fields of  $\overline{\Phi}$  and  $\overline{\Phi}_m$  for case 10M. Note that log scale is used.

netic energy  $\overline{\Phi}$  and its mean part  $\overline{\Phi}_m$  are presented in Fig. 13. The field structure already observed on the reference mesh (Fig. 5) is recovered also on the coarse mesh with the only difference being the magnitude of dissipation which is (as ex-

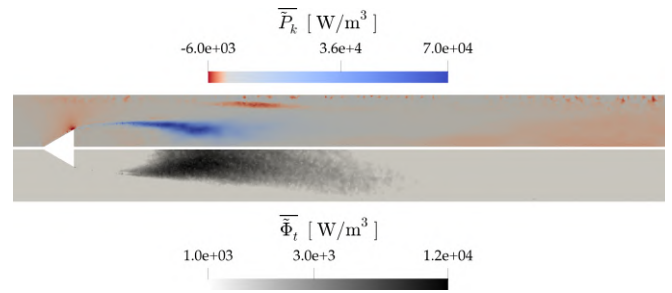


FIG. 14. QOI fields of  $\overline{P}_k$  and  $\overline{\Phi}_t$  for case 10M. Note that log scale is used only for  $\overline{\Phi}_t$  field.

pected) higher with the coarse mesh. As a result, dissipation of mean kinetic energy happens mainly at the wall boundary-layer and in the shear-layer of the bluff-body.

Dissipation rate of turbulent kinetic energy  $\overline{\Phi}_t$  is presented in Fig. 14 together with the production rate  $\overline{P}_k$ . As on the reference mesh,  $\overline{\Phi}_t$  is large in the wake of the bluff-body and  $\overline{P}_k$  exhibits a negative (red) region at the flame-holder corner (where turbulent kinetic energy is transferred to the mean field) and a positive (blue) region in the shear-layer (where mean kinetic energy is transferred to turbulence).

From the aerodynamics QOI fields, the LIKE criterion (Eq. (6)) is at first used to build a refinement metric. As a results from the comparison between the different QOI's, a value of  $\alpha$  of 1 is selected, together with a  $\varepsilon$  of 0.5 to avoid refining too much in small regions. The resulting mesh of 17M did not provide satisfactory accuracy in the aerodynamic field prediction (results not shown) and the same procedure is applied again resulting in the 29M mesh shown in Fig. 15. A correct prediction of the flame shape which now extends once

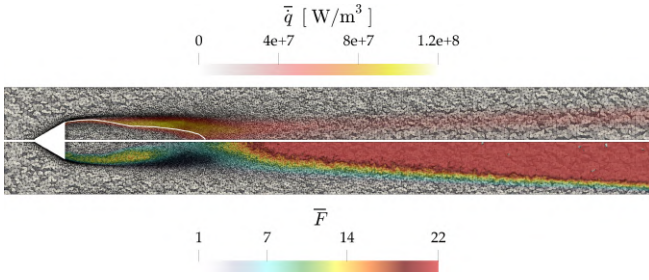


FIG. 15. Overview of the 29M mesh obtained after the aerodynamics second refinement step using LIKE criterion. Time-averaged heat release rate  $\bar{q}$  and thickening factor field  $\bar{F}$  are superimposed to the grid. The white iso-contour delimits the recirculation zone ( $U_x = 0$  m/s).

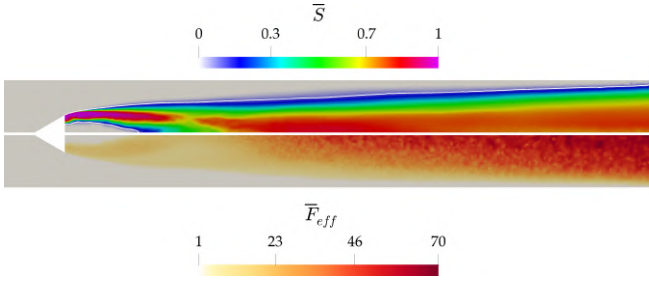


FIG. 16. QOI fields of flame probability  $\bar{S}$  and the effective thickening  $\bar{F}_{eff}$  for case 29M. The white iso-contour correspond to  $\bar{S} = 0.1$ .

again until the end of the combustion chamber is achieved as it is possible to observe from the averaged heat release rate  $\bar{q}$  and thickening factor field  $\bar{F}$ . This indicates that the refinement of the shear-layer achieved with the aerodynamic QOI's increases the accuracy of the prediction of the velocity gradients in these regions allowing the presence of the flame as in the experiments. Nevertheless, the maximum thickening factor obtained with this 29M mesh is still too high if compared to the reference case especially at the end of the burner. This may cause an incorrect estimation of the flame-turbulence interaction especially if the characteristic length of turbulence across the computational domain is changing due to turbulence production/dissipation<sup>41</sup>.

As before, to improve the resolution in the flame region, the FET flame criterion is used. QOI fields of flame probability  $\bar{S}$  and the effective thickening  $\bar{F}_{eff}$  are showed in Fig. 16 and used to build the FET criterion.

The *a priori* estimation of the number of cells (Eq. (15)) is then used to chose  $\bar{F}_{target}$  and  $\bar{S}_{limit}$ . The obtained curves are showed in Fig. 17. With the objective to achieve the same cost as the previously discussed optimized 45M mesh, a  $\bar{F}_{target}$  of 15 and a  $\bar{S}_{limit}$  of 0.1 are selected. Note that for low values of  $\bar{S}_{limit}$  the cells number do not change significantly because the region where  $\bar{F}_{eff}$  is large (i.e. where refinement is of interest) corresponds to a region where  $\bar{S}$  is large (see Fig. 16) and it is always identified if  $\bar{S}_{limit}$  is sufficiently small.

The resulting 46M mesh is shown in Fig. 18, together with the averaged heat release rate  $\bar{q}$  and thickening factor field  $\bar{F}$ .

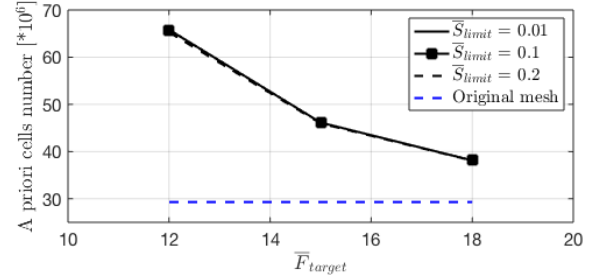


FIG. 17. A priori computation of the refined mesh cells number for case 29M ad a function of  $\bar{F}_{target}$  and the  $\bar{S}_{limit}$ .

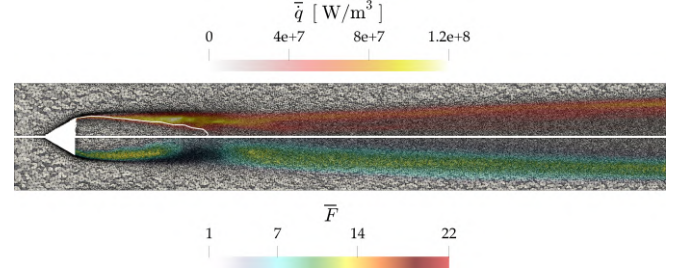


FIG. 18. Overview of the 46M mesh obtained after the combustion refinement step mesh by using the FET criteria ( $\bar{F}_{target} = 15$ ,  $\bar{S}_{limit} = 0.1$ ). Averaged heat release rate  $\bar{q}$  and thickening factor field  $\bar{F}$  are superimposed to the grid. The white iso-contour delimits the recirculation zone ( $U_x = 0$  m/s).

Comparison with the 29M mesh (Fig. 15) shows a large improvement in the resolution of the flame in the last part of the domain, visible as a much more homogeneous and small thickening factor  $\bar{F}$ .

The improvement of the LES accuracy thanks to the refinement procedure is clearly visible if comparing the data against the LES using the 10M (coarse), 29M (only aerodynamic refinement), 46M (optimum mesh) and 68M (reference) meshes in Fig 19. Axial profiles of the mean axial velocity component are presented in Fig 19(a). The accuracy of the axial velocity prediction increases with the refinement steps. Starting from an incorrect solution where the recirculation zone length is over-predicted and the burnt gas acceleration is under-predicted (cf. case 10M), the method is able to recover both the correct mean aerodynamic and reactive fields and provides as accurate results as the reference case with a much lighter mesh. The mesh refinement quality is valid for the entire extension of the computational domain and not only at the center line of the burner as observed in Fig 19(b) where the transverse profiles of the mean normalized axial velocity are reported. Another key feature concerns the turbulent behaviour of the flow. Obviously, the 10M mesh is not able to accurately predict the turbulence activity. Figure 19(c-d) reports the transverse profiles of normalized RMS of the axial and transverse velocity from  $x_1$  to  $x_5$  respectively. The refinement process is able to recover the turbulent activity of the flow as well as for the mean aerodynamic field. Also note that the refinement quality is homogeneous since the axial and

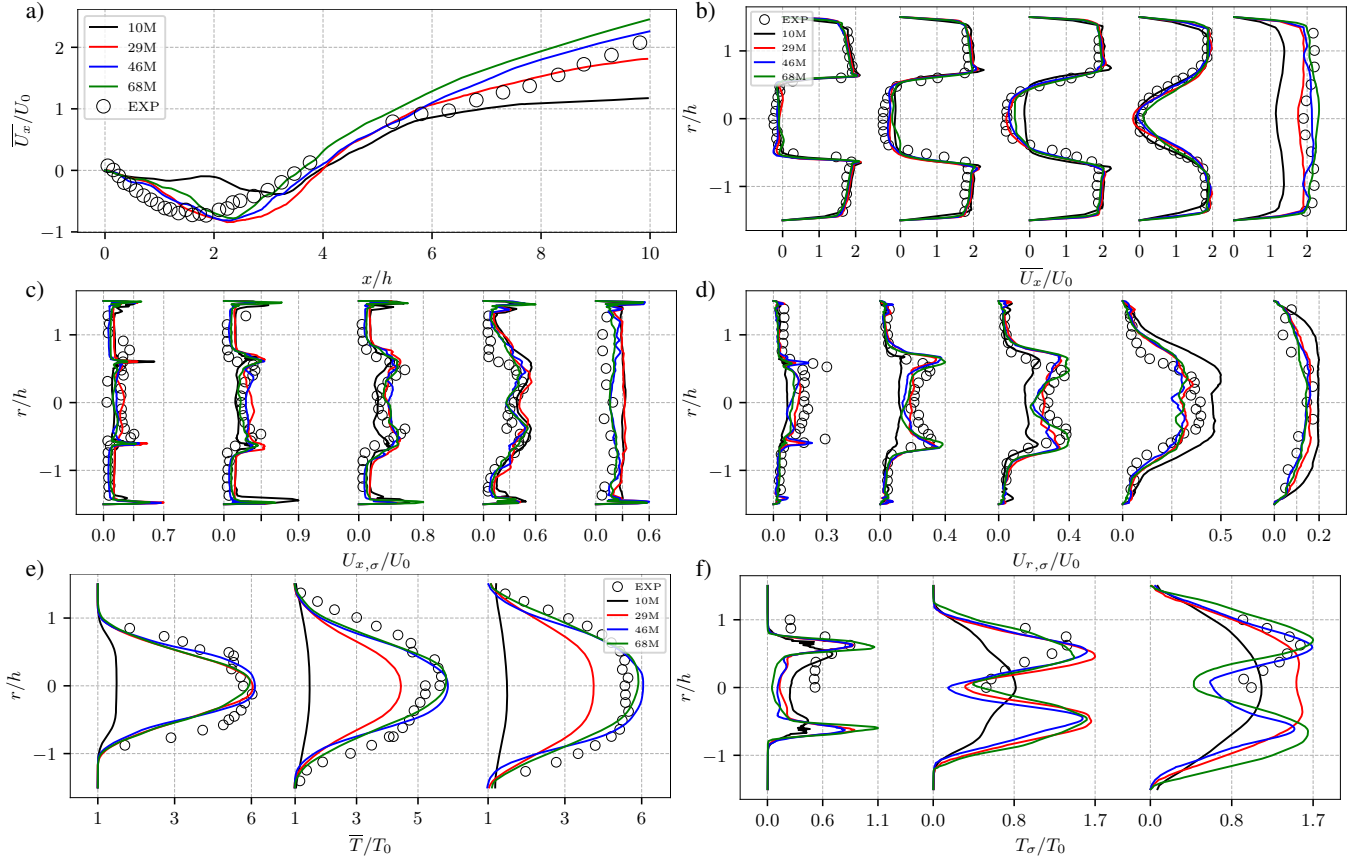


FIG. 19. Comparison between experimental data and LES for the 10M, 29M, 46M and 68M (reference) cases. Mean axial velocity evolution along the central axis (a). Transverse profiles at measurement planes  $x_1 - x_5$  of the mean normalized axial velocity (b), the normalized RMS of axial velocity component (c) and the normalized RMS of transverse velocity component (d). Transverse profiles of normalized mean temperature (e) at measurement planes  $x_4$ ,  $x_4'$  and  $x_5'$  and its normalized RMS (f) at measurement planes  $x_2$ ,  $x_4$  and  $x_5$ .

transverse turbulent fluctuations are evenly accurate. In addition to the velocity results, the averaged transverse temperature profiles presented in Fig. 19(e) confirm the good prediction of the mean reactive flow. Note that the correct profiles are only recovered at the ultimate refinement step, i.e. using the flame criterion, while the aerodynamic refinement shows good accuracy just downstream the bluff-body. Finally, Fig. 19(f) shows the normalized RMS transverse temperature profiles. The flame/turbulence interaction is also well predicted with the optimum mesh, i.e., the one where the FET criterion is used.

#### IV. A PARTIALLY PREMIXED SWIRLED FLAME: THE PRECCINSTA TEST BENCH

The proposed mesh refinement strategy is here applied to the gas turbine model combustor PRECCINSTA, a well-known gas turbine model combustor derived from an industrial design by Safran Helicopter Engines and operated by DLR.<sup>45</sup> A schematic of the experimental test bench is shown in Fig. 20(a)<sup>45</sup>, presenting the injector with the combustion chamber together with an image of the flame. Dry air is fed at ambient temperature through the plenum and a swirl mo-

tion is imposed before the combustion chamber thanks to 12 radial swirler vanes. The test bench is a partially (i.e. technically) premixed case, since the fuel gas ( $\text{CH}_4$ ) is injected into the air stream through small holes within the radial swirler. The high momentum ensures good mixing before entering the combustion chamber even if local equivalence ratio variations have been reported in the literature.<sup>45</sup> The combustion chamber has a 85 mm large squared section and it is delimited by large quartz windows of thickness 1.5 mm which allow for optical access for diagnostics. Finally the hot gases exit through a cone-shaped exhaust pipe.

This configuration has been widely described and studied both experimentally<sup>69-72</sup> and also numerically<sup>4,5,46,73-80</sup>. Most of the studies refer to the two regimes experimentally observed by Meier *et al.*<sup>69</sup>: for a global equivalence ratio of  $\phi = 0.7$  (thermal power  $P_{th} = 25$  kW) an unstable flame with a thermoacoustic limit cycle at 290 Hz is detected while, for a global equivalence ratio of  $\phi = 0.83$  ( $P_{th} = 30$  kW) a quiet and stable flame is obtained. The thermoacoustic behavior of the flame has been numerically analyzed via compressible LES by Franzelli *et al.*<sup>73</sup> who also analyzed the impact of detailed chemistry on the LES accuracy<sup>74</sup>. A fully-compressible LES-pdf approach, originally developed by Gao and O'Brien<sup>81</sup>, comprising the Eulerian stochastic

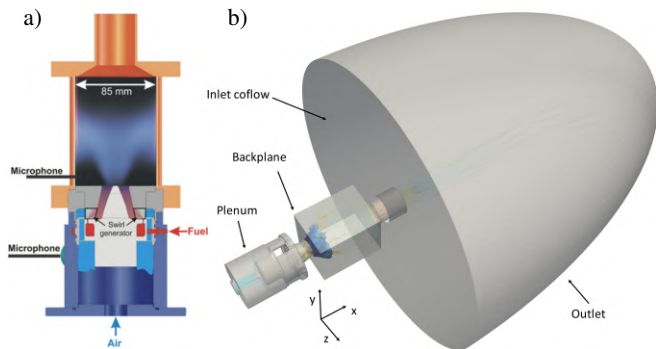


FIG. 20. Schematic of the experimental test bench: injector with combustion chamber and photo of the flame (a)<sup>45</sup>. Computational domain used in LES (b). Note that in LES the atmosphere is taken into account and the inlet fuel geometry is simplified to the 12 small tubes without the fuel plenum.

fields methods has been proposed by Friedrich *et al.*<sup>75,80</sup> to detect the thermo-acoustic instability. A mesh refinement study has been only recently proposed by Bénard *et al.*<sup>46</sup>. The latter focuses on the stable case  $\phi = 0.83$  and analyses via incompressible LES the effect on the flame structure of 4 homogeneously refined meshes ranging from 1.7 M cells (the coarsest mesh) to 110M and 877 M cells (the most refined ones), which leads to a  $F_{max}$  of 5.7 and 3.3, respectively. Following the choice of Bénard *et al.*<sup>46</sup> in this section the proposed mesh refinement strategy is applied to the stable flame, avoiding additional complexities due to thermoacoustic oscillations. Note that the method is perfectly suitable for applications to unstable flames if the defined QOI are time-averaged for longer times if compared to thermoacoustic oscillations.

The good quality and the extensive amount of experimental data available for the selected operating case in addition to its industrial-like design makes the PRECCINSTA test bench very suitable for the application of the proposed mesh refinement strategy. In particular, for what regards the aerodynamic field, measurements of the three velocity components were performed in one vertical plane along radial profiles at the heights  $h = 1.5, 2.5, 5, 15, 25$  and  $35$  mm from the backplane using Laser Doppler velocimetry<sup>69</sup>. The uncertainty of the velocity measurements is typically 1.5–2% for the mean value and 2–2.5% for the RMS value. To check the accuracy of flame prediction, Laser Raman scattering experimental data<sup>69</sup> are available providing quantitative measurements of major species ( $\text{CH}_4, \text{O}_2, \text{N}_2, \text{CO}, \text{CO}_2, \text{H}_2\text{O}$  and  $\text{H}_2$ ) and temperature in the vertical  $xy$  plane at different sections downstream the backplane ( $h = 6, 10, 15, 20, 30, 40, 60$  and  $80$  mm). The systematic and statistical uncertainties are less than 4% and 2.5% respectively for temperature and less than 5% and 7% respectively for all species, except for  $\text{CO}$  and  $\text{H}_2$  for which the statistical uncertainty is between 20% and 50%. In addition, PLIF of OH radicals was applied to visualize the flame structures together with line-of-sight integration of OH\* chemiluminescence, which represents a qualitative indicator for the heat release rate for lean premixed flames.

LES are performed considering the computational domain

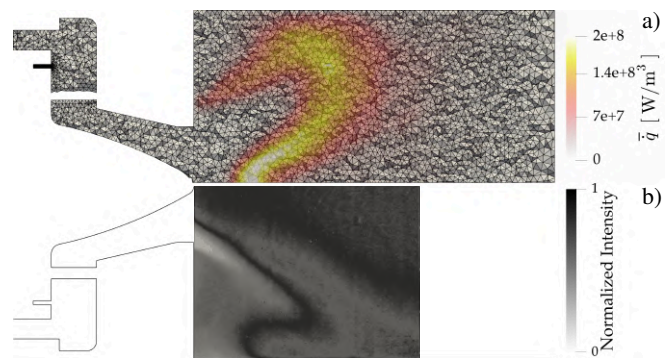


FIG. 21. (a) Overview of the 3M coarse mesh. The characteristic mesh size  $\Delta x$  of 1.2 mm corresponds to the coarse mesh resolution proposed by Bénard *et al.*<sup>83</sup>. The flame is represented through an averaged field of heat release rate  $\bar{q}$ . (b) Experimental normalized time-averaged OH PLIF image<sup>69</sup>.

shown in Fig. 20(b) and using the same numerical method as for the VOLVO test case (Sec.III). Thermal boundary conditions are imposed by fixing a reference temperature  $T_{ref}$  and a suitable thermal resistance. At the bluff-body and at the backplane, thermal resistances are imposed based on experimental work by Yin *et al.*<sup>72</sup> that provided the surface temperature for operating conditions of thermal power  $P_{th} = 20\text{KW}$  and equivalence ratio  $\phi = 0.7$ . The latter condition has been simulated in AVBP and the thermal resistances have been tuned to match the experimental thermal profiles, assuming that the thermal resistance does not change while changing operating conditions (while surface temperature of course does). The same procedure has been applied for the chamber walls, based on the flow thermal profiles measured by Meier *et al.*<sup>69</sup>. The others walls are assumed to be adiabatic since no heat transfer is expected and no-slip conditions are imposed for all the walls. Since the current approach does not take into account the experimentally observed pre-heating of the flow in the plenum, a temperature of the flow of 320K is imposed at the inlet as generally proposed in the literature and also as  $T_{ref}$  for the walls thermal boundary conditions. The flame is modeled with the Thickened Flame model (TFLES), as in the VOLVO test case. In order to better take into account the local equivalence ratio variation due to the partially premixed case, the  $\text{CH}_4$ -Air chemistry is described by an ARC mechanism comprising 20 species, 166 reactions, and 9 quasi-steady state species derived from the GRI-Mech 3.0 and validated by Laera *et al.*<sup>82</sup>.

## A. Results and discussion

The starting mesh is shown in Fig. 21. It is composed by 2.8M of cells and it is homogeneously refined in the combustion chamber and in the swirler zone with a characteristic mesh size  $\Delta x$  of 1.2 mm which corresponds to the coarse mesh resolution proposed by Bénard *et al.*<sup>83</sup>. Note that the small tubes for technically premixed fuel injection are discretized with 8 cells in the diameter (i.e. 0.125 mm of characteristic

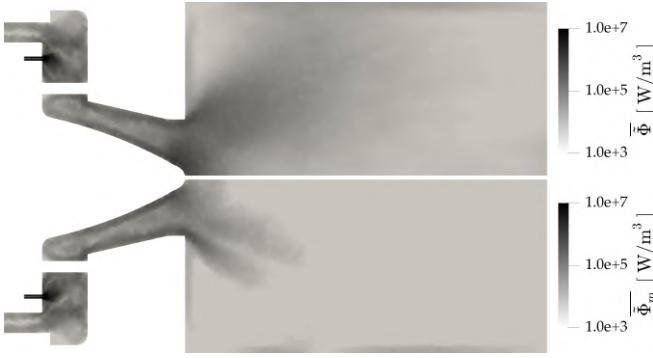


FIG. 22. QOI fields of  $\bar{\Phi}$  and  $\bar{\Phi}_m$  for 3M coarse mesh. Note that log scale is used.

size), corresponding to the smallest cells in the domain and to the largest CFL number. To avoid decreasing too much the timestep  $\Delta t$  of the compressible LES code, no mesh refinement is allowed in this region of the domain, assuming that a sufficient resolution for computing the jet penetration in the air flow is achieved with the current mesh size. The averaged heat release rate  $\bar{q}$  is superimposed to the mesh in Fig. 21(a). Due to a poor mesh resolution, the flame shape is totally wrong compared to the experimental time-averaged OH PLIF image (b): the flame has an M-shape, as opposed to the experimental data which show a clear V-shape, with the flame attached to the bluff-body and detached from the back-plane. The wrong shape prediction is due to double effect induced by the low resolution. On one side the velocity field prediction is not accurate enough and, on the other side, the flame has an artificial thickness which is of the order of the bluff-body tip diameter: therefore the flame cannot stabilize close to the bluff-body tip since the two flames branches typical of a V-shape touch each other and merge in a M-flame. Temperature boundary condition does not impact the flame shape transition since increasing the  $T_{ref}$  of the bluff body does not lead to a V-shape flame.

As shown in the VOLVO test case, starting from this initial arbitrary mesh and solution, an optimum mesh with improved accuracy can be obtained by following the proposed mesh refinement strategy (Sec.III A 2). First, aerodynamics QOI are computed. Total dissipation rate of kinetic energy  $\bar{\Phi}$  and its mean part  $\bar{\Phi}_m$  are presented in Fig. 22.  $\bar{\Phi}_m$  happens mainly in the small tubes and at the bluff body and swirler walls. Important dissipation is present also at the jet shear-layer.  $\bar{\Phi}$  field is as expected very close in terms of magnitude and structure to its mean part, the only difference being the region at the bluff-body tip and in the jet core which correspond to region of dissipation of turbulent kinetic energy  $\bar{\Phi}_t$ . The latter is presented in Fig. 23 together with the production  $\bar{P}_k$ .  $\bar{\Phi}_t$  is large in the wake of the bluff-body and  $\bar{P}_k$  exhibits a negative (red) region at the bluff-body tip (where turbulent kinetic energy is transferred to the mean field) and a positive (blue) region in the shear-layer (where mean kinetic energy is transferred to turbulent one).

From the comparison between the different QOI's, a value

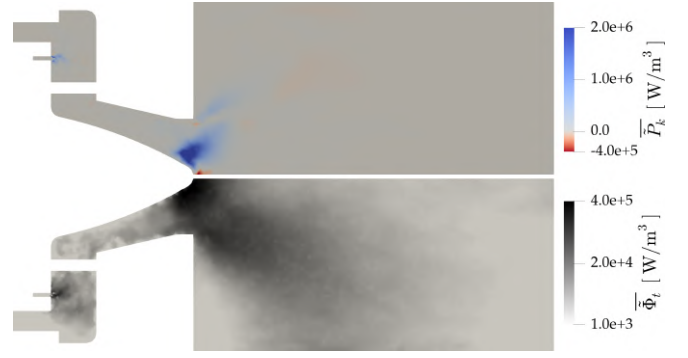


FIG. 23. QOI fields of  $\bar{P}_k$  and  $\bar{\Phi}_t$  for 3M coarse mesh. Note that log scale is used only for  $\bar{\Phi}_t$  field.

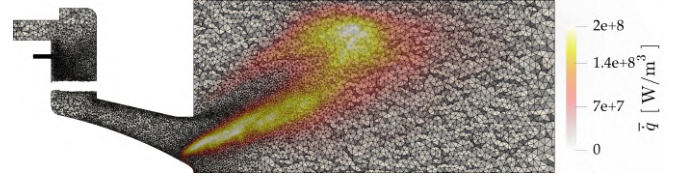


FIG. 24. Overview of the 10M mesh. The flame is represented through an averaged field of heat release rate  $\bar{q}$ .

of  $\alpha$  of 5 is selected in order to flag regions of dissipation and production of turbulent kinetic energy which cannot be identified with a lower  $\alpha$  parameter, due to the different order of magnitude of the different QOI's. Also in this case, a  $\epsilon$  parameter of 0.5 is used to avoid over-refining in small regions.

Fig. 24 shows the mesh obtained after two refinement steps using aerodynamics  $\bar{\Phi}$  field as QOI. An intermediate mesh of 5M is obtained after one iteration which, however, was not sufficient to guarantee a satisfactory accuracy in the aerodynamic field prediction. The achieved 10M mesh exhibits smaller cells and hence higher accuracy near the swirler and the bluff-body walls and also in the jet shear-layer and jet-core where most of the aerodynamics activity happens.

The resulting averaged heat release rate  $\bar{q}$  corresponds to a correct V-shape flame, confirming that the refinement of the mesh in the shear-layer with the aerodynamic QOI is able to increase the accuracy of aerodynamics field prediction and to recover the correct flame shape. The LES prediction of the velocity field is in very good agreement with the experimental data (see Fig. 27). However, in order to improve the resolution in the flame region, the FET flame criterion is used to refine the 10M mesh in the reactive region. QOI fields of flame probability  $\bar{S}$  and the effective thickening  $\bar{F}_{eff}$  are shown in Fig. 25 and used to build the FET criterion.

The white iso-contour corresponds to an  $\bar{S}_{limit}$  of 0.1 that delimits the flame region where the FET criterion is applied. As there is no special target in terms of mesh cells number, the  $\bar{F}_{target}$  is chosen in order to directly compare with the resolution of Bénard *et al.*<sup>46</sup>. The higher resolution achieved in their analysis bring to a  $\bar{F}_{max}$  applied of 5.7 and 3.3 with 110M and 877 M cells respectively. By using the FET criterion with a  $\bar{F}_{target}$  of 3.3 and 5.7 will bring to meshes of  $\approx 22$  M and

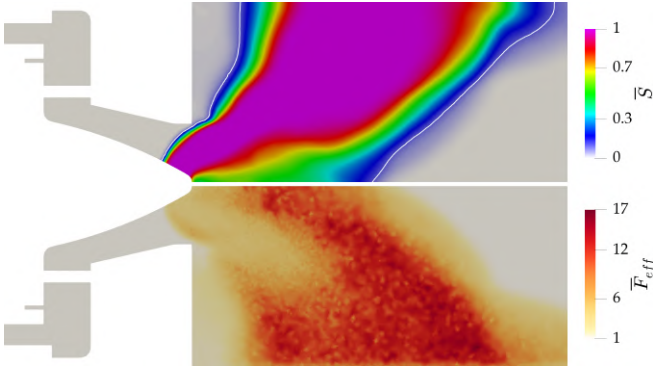


FIG. 25. QOI fields of flame probability  $\bar{S}$  and the effective thickening  $\bar{F}_{eff}$  for case 10M. The white iso-contour corresponds to  $\bar{S} = 0.1$ .

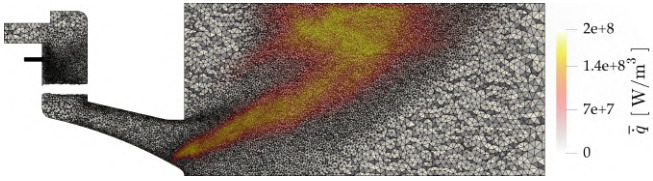


FIG. 26. Overview of the 22M mesh. The flame is represented through an averaged field of heat release rate  $\bar{q}$ . The  $\bar{F}_{target}$  of 5.7 assures same resolution in the flame region as in the 110 M cells mesh by Bénard et al.<sup>46</sup>

$\approx 100$  M cells respectively, following the a-priori calculation. For the present analysis, an  $\bar{F}_{target}$  of 5.7 is selected in order to have the same resolution of the NAD3 mesh<sup>46</sup>. The resulting mesh is showed in Fig. 26 and is composed by 22M of cells, underlying how it is possible to efficiently build high resolution meshes by using a mesh refinement strategy based on physical QOI.

The final mesh shows very good agreement with the experimental data, both in terms of velocity field and flame prediction. In particular, profiles of velocity components at different measurement planes for the 3M, 5M, 10M and 22M meshes are showed in Fig. 27. Mean axial velocity Fig. 27(a) is wrongly predicted only by the coarse case (3M), which predicts a shorter recirculation zone. Some differences between LES and experiments remain visible at  $h = 15$  and 25 mm downstream the backplane, suggesting that the opening angle is slightly under-predicted, and can be explained by taking into consideration the uncertainty of the experimental data. The corresponding RMS instead are over-estimated also by the 5M case, while the 10M and the 22M case are in good agreement with the experimental data. For what regards the mean radial velocity Fig. 27(c) and tangential velocity Fig. 27(e) again the coarsest mesh is the only one that does not provide very accurate results, indicating the first step of aerodynamic mesh refinement (i.e. 5M mesh) is able to improve the mean aerodynamic flow prediction. On the contrary, by looking at the radial velocity Fig. 27(d) and tangential velocity RMS Fig. 27(f), it is evident that the 5M case overestimates the turbulent activity and that a second refinement step (i.e. 10M mesh) is mandatory to recover the experimen-

tal behavior.

The accuracy of flame prediction can be inferred from Fig. 28 where the profiles of temperature and selected species at different measurement planes are shown for the 3M, 5M, 10M and 22M meshes. Mean temperature profiles Fig. 28(a) show good accuracy of the 10M and 22M meshes with experimental data, only marginal agreement of the 5M case and wrong prediction of the 3M case since the predicted flame shape is wrong. Some differences between LES and experiments remain visible also in this case at  $h = 15$  and 25 mm downstream the backplane and can be explained by taking into consideration the uncertainty of the experimental data and the tuning procedure of the imposed thermal boundary conditions at the chamber walls. The RMS Fig. 28(b) are perfectly recovered by the refined meshes, confirming that two steps of aerodynamic refinement are needed for good prediction of aerodynamic activity. Selected species are  $H_2O$  and  $CO$  (but the same trend apply to the others). Mean Fig. 28(c) and RMS Fig. 28(d) of  $H_2O$  mass fraction show good agreement of the refined meshes (10M and 22M). Mean Fig. 28(e) and RMS Fig. 28(f) of  $CO$  mass fraction instead show that the 10M mesh is not able to correctly predict the minimum of mean value and activity along the axis while the 22M mesh is able to correctly recover the experimental data. This shows that when considering weak species (note the magnitude of mass fraction) the mesh resolution in the flame can play an important role for the LES accuracy prediction.

Finally, in Fig. 29 the instantaneous flames computed on the 3M (a), 5M (b), 10M (c) and 22M (d) meshes are presented. The flames are identified by iso-surfaces of  $\dot{q} = 10\% \dot{q}_{max}$  colored by the instantaneous thickening field  $F$  (on the left) and the temperature field  $T$  (on the right). The difference of predicted flame-shape and length for the different mesh resolution is evident. The coarse 3M mesh (a) predicts an M-shape flame that does not touch the bluff-body tip and that is very close to the chamber backplane. The applied thickening is in the order of 16, bringing to an artificial flame thickness which is comparable to the bluff-body tip. As a consequence, the flame is detached and a large-scale hydrodynamics structure (the Precessing Vortex Core) can be detected by an iso-surface of low pressure<sup>8,84</sup>. The PVC spiral structure is often detected in the PRECCINSTA burner when the flame has an M-shape while when a V-shape is present no PVC is detected<sup>85,86</sup>. In experiments, depending on the operating conditions (i.e. thermal power  $P_{th}$  and equivalence ratio  $\phi$ ) the flame can either assume an attached V-shape with no PVC, a detached M-shape with PVC or a bi-stable behavior alternating intermittently between V- and M-shape. In the current operating conditions, the flame has a V-shape: it is therefore interesting to notice that the predicted M-shape is due to the poor mesh resolution and that the PVC is fictitious. The correct flame shape is recovered just after the first step of aerodynamic refinement with the 5M mesh (Fig. 29(b)), with the suppression of the PVC. The applied thickening factor is now halved in the region where mesh refinement has been applied, bringing to a lower artificial flame thickness. As the mesh refinement procedure goes on, the new 10M mesh Fig. 29(c) exhibits lower applied thickening and more accurate flame-turbulence inter-

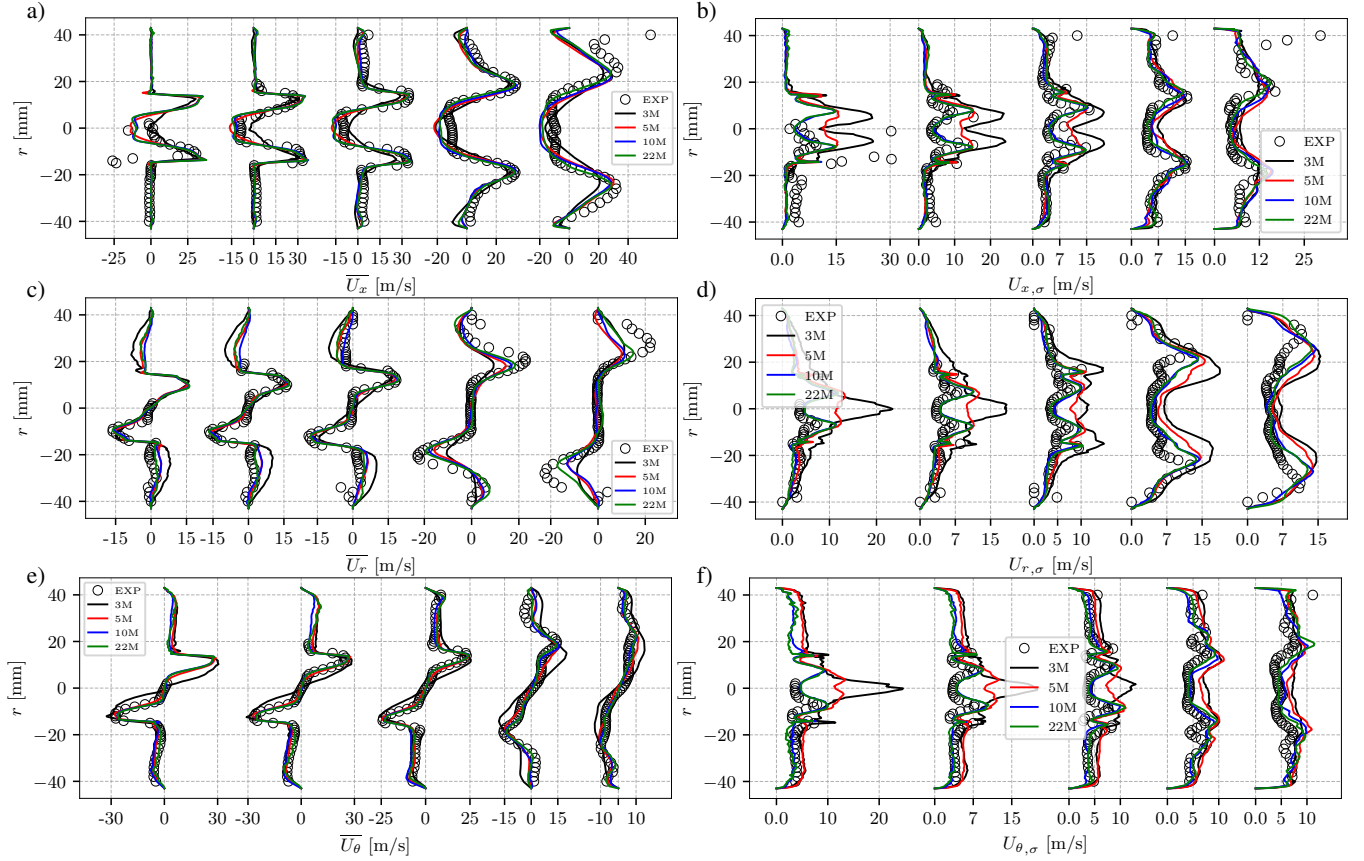


FIG. 27. Profiles of velocity components at measurement planes at  $h = 1.5, 2.5, 5, 15, 25$  mm downstream the backplane for the 3M, 5M, 10M and 22M cases. Mean (a) and RMS (b) axial velocity. Mean (c) and RMS (d) radial velocity. Mean (e) and RMS (f) tangential velocity.

action and turbulent activity prediction. The final step of the 22M mesh (Fig. 29(d)) shows that the instantaneous thickening is lower than the  $F_{target} = 5.7$  except for the small portion of the flame near the backplane where the flame goes only for less than the 10% of the time (i.e.  $S_{limit} = 0.1$ ). Finally, the resulting mesh exhibits a much more homogeneous applied thickening, and hence resolution in the flame, confirming that the method takes into account possible local variation in equivalence ratio due to the technical injection (see the instantaneous iso-surface of  $\text{CH}_4$  mass fraction in (Fig. 29(d)). Note that an effect of the mesh resolution on the flame lift-off is visible. In particular, as observed in literature<sup>46</sup>, an increase of the mesh resolution brings to an increase of the flame lift-off from the backplane, due to the improved prediction of flame response to stretch when an improved-resolution mesh is used.

## V. CONCLUSIONS

A new static mesh refinement strategy based on physical Quantities of Interest (QOI) has been proposed in LES of turbulent reactive flows. To define the regions of interest (ROI) where relevant flow physics happens, different QOI's have been defined for the aerodynamic field and for the flame. Analysis of the balance equation for the mean and the turbu-

lent kinetic energies have shown that the dissipation rate of the mean and the turbulent kinetic energy together with the production of turbulent kinetic energy have to be taken into account to correctly capture the flow activity. In addition, from the reactive flow point of view, a criterion based on the flame-position probability and on the effective applied thickening has been defined to obtain the desired mesh resolution in the flame region. At first, this mesh refinement strategy has been successfully applied and validated on the VOLVO test case: an academic fully premixed bluff-body stabilized flame. The method was able to correctly define the ROI where important physics happen: it was possible to locally refine the mesh in this region to improve the LES prediction accuracy or, alternatively, to fix the mesh size in this region and coarsen everywhere else in the domain to reduce the mesh size and hence the computation cost while keeping the same LES accuracy of a reference mesh. By comparing the results with the experimental data, it was evident that the prediction of the flame stabilization, and hence the computed velocity and temperature fields, are strongly influenced by the mesh quality that can be significantly improved by applying the proposed mesh refinement strategy. On the starting mesh, the flame was short and burnt inside the wake of the flame-holder and a long recirculation zone was predicted. The final mesh instead predicted a long flame which burned for the whole combustion chamber downstream the bluff-body, as in the experiments. Second,

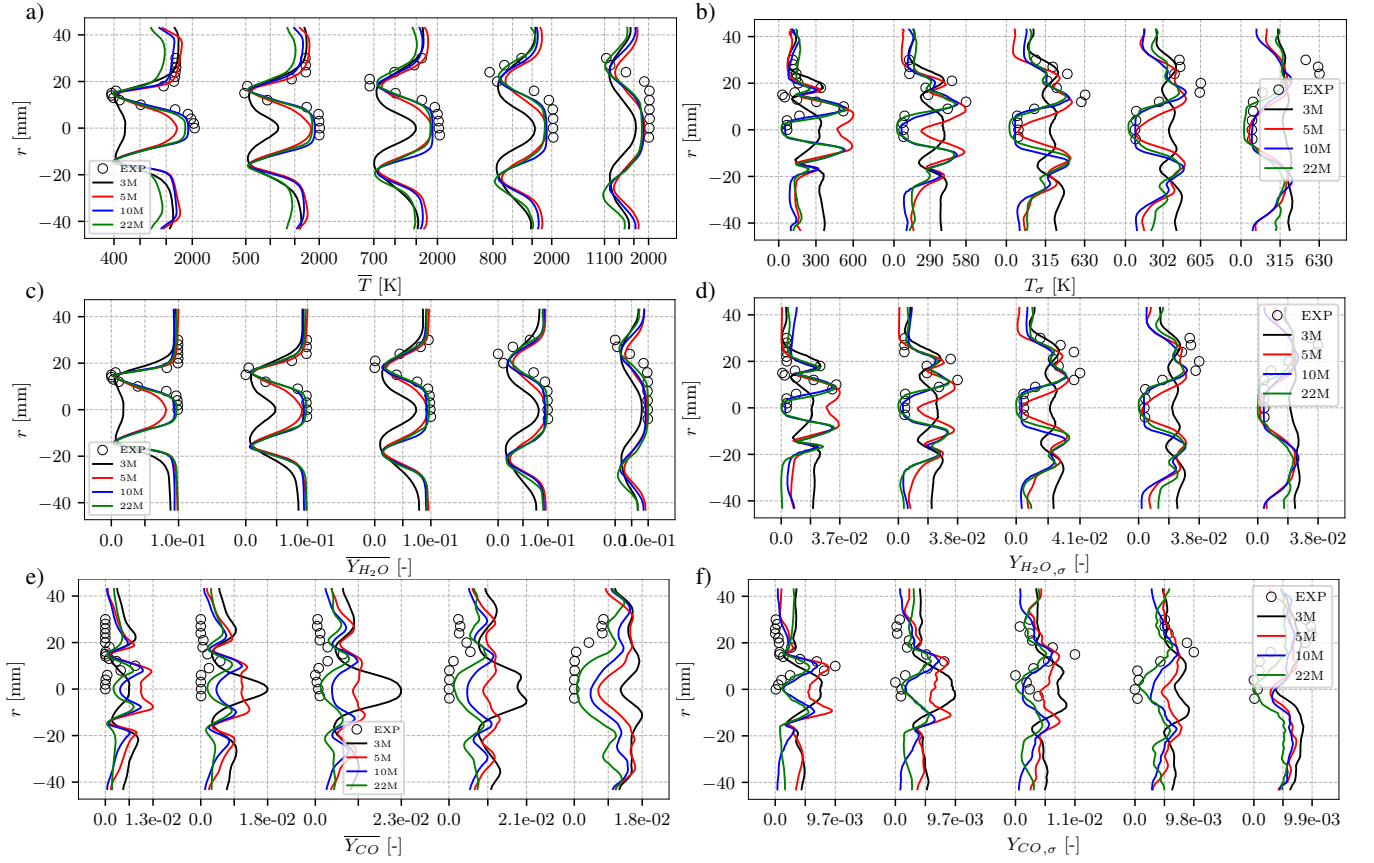


FIG. 28. Profiles of temperature and selected species at measurement planes at  $h = 6, 10, 15, 20$  and  $30$  mm downstream the backplane for the 3M, 5M, 10M and 22M cases. Mean (a) and RMS (b) temperature. Mean (c) and RMS (d)  $H_2O$  mass fraction. Mean (e) and RMS (f) CO mass fraction.

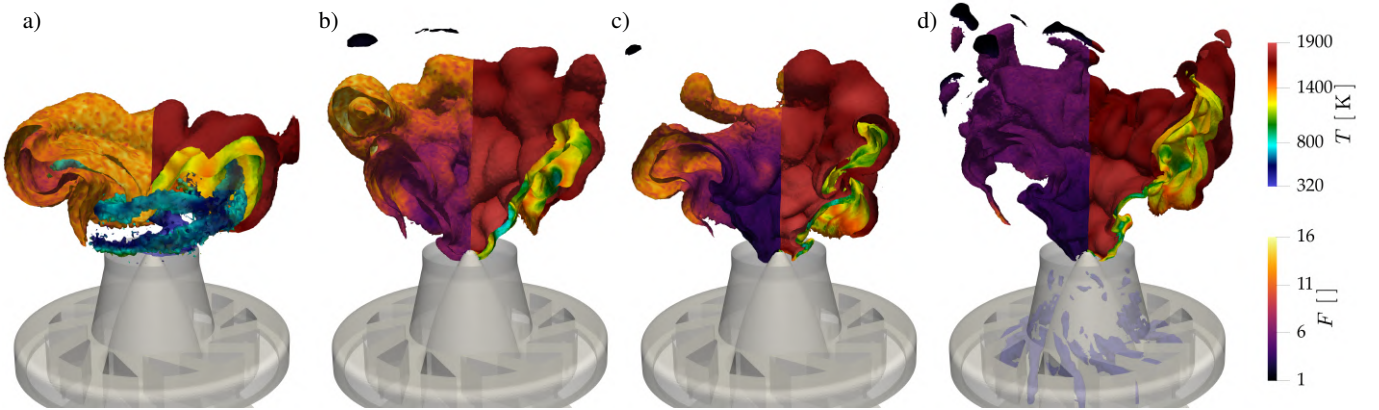


FIG. 29. Iso-surfaces of  $\dot{q} = 10\% \dot{q}_{max}$  colored by thickening field  $F$  (on the left) and temperature field  $T$  (on the right) for the 3M (a), 5M (b), 10M (c) and 22M (d) meshes. For the 3M case, an iso-surface of pressure at 101 kPa (colored by temperature field) evidences the Processing Vortex Core (PVC) present when the flame has an M-shape. For the 22M case, instantaneous iso-surface of  $CH_4$  mass fraction equal to 0.08 colored by temperature field.

the method has been applied to a partially premixed swirler flame which is closer to the real industrial configurations, the PRECCINSTA test bench. Also in this case, it was possible to obtain a predicted V-shape flame in very good agreement with the experimental data starting from a wrong predicted

M-shape flame. The key point of the proposed method relies in its versatility: in both the test cases the strategy was able to lead to a correct solution in very good agreement with the experiments starting from a totally wrong initial solution. Therefore, the proposed mesh refinement strategy is found to

be able to identify the relevant physics of turbulent reacting flows that are essential for the overall LES accuracy.

## ACKNOWLEDGMENTS

This project has received funding from the H2020-MSC-ITN Grant Agreement No 766264 (MAGISTER), the MSCA Grant Agreement No 843958 (CLEANERFLAMES - D. L. Individual Fellowship) and the H2020 Grant Agreement 952181 (COEC - Center of Excellence in Combustion). HPC resources from the PRACE Project 2020225434 (FANTASTIC-H2) are also acknowledged. The authors would also like to thank Stephane Richard from Safran Helicopter Engines (SHE) for valuable discussions and Wolfgang Meier from the German Aerospace Center (DLR) for providing the PRECCINSTA rig experimental data.

## DATA AVAILABILITY

The data that support the findings of this study are available from the corresponding author upon reasonable request.

- 1 U. Piomelli, "Large-eddy simulation: achievements and challenges," *Prog. Aerosp. Sci.* **35**, 335–362 (1999).
- 2 C. Yu, Z. Xiao, and X. Li, "Scale-adaptive subgrid-scale modelling for large-eddy simulation of turbulent flows," *Phys. Fluids* **29**, 035101 (2017).
- 3 M. H. Silvis, R. A. Remmerswaal, and R. Verstappen, "Physical consistency of subgrid-scale models for large-eddy simulation of incompressible turbulent flows," *Phys. Fluids* **29**, 015105 (2017).
- 4 S. Roux, G. Lartigue, T. Poinso, U. Meier, and C. Bérat, "Studies of mean and unsteady flow in a swirled combustor using experiments, acoustic analysis, and large eddy simulations," *Combust. Flame* **141**, 40–54 (2005).
- 5 V. Moureau, P. Domingo, and L. Vervisch, "From large-eddy simulation to direct numerical simulation of a lean premixed swirl flame: Filtered laminar flame-pdf modeling," *Combust. Flame* **158**, 1340–1357 (2011).
- 6 Y. Huang, H.-G. Sung, S.-Y. Hsieh, and V. Yang, "Large-eddy simulation of combustion dynamics of lean-premixed swirl-stabilized combustor," *J. Propul. Power* **19**, 782–794 (2003).
- 7 P. W. Agostinelli, Y. H. Kwah, S. Richard, G. Exilard, J. R. Dawson, L. Gicquel, and T. Poinso, "Numerical and experimental flame stabilization analysis in the new spinning combustion technology framework," *ASME Turbo Expo*, (2020).
- 8 L. Y. Gicquel, G. Staffelbach, and T. Poinso, "Large eddy simulations of gaseous flames in gas turbine combustion chambers," *Prog. Energ. Combust.* **38**, 782–817 (2012).
- 9 P. Wolf, R. Balakrishnan, G. Staffelbach, L. Y. Gicquel, and T. Poinso, "Using les to study reacting flows and instabilities in annular combustion chambers," *Flow Turbul. Combust.* **88**, 191–206 (2012).
- 10 P. Wolf, G. Staffelbach, A. Roux, L. Gicquel, T. Poinso, and V. Moureau, "Massively parallel les of azimuthal thermo-acoustic instabilities in annular gas turbines," *Comptes Rendus Mecanique* **337**, 385–394 (2009).
- 11 E. L. Schiavo, D. Laera, E. Riber, L. Gicquel, and T. Poinso, "Effects of liquid fuel/wall interaction on thermoacoustic instabilities in swirling spray flames," *Combust. Flame* **219**, 86–101 (2020).
- 12 Y. Sommerer, D. Galley, T. Poinso, S. Ducruix, F. Lacas, and D. Veynante, "Large eddy simulation and experimental study of flashback and blow-off in a lean partially premixed swirled burner," *J. Turbul.* **5**, 1–3 (2004).
- 13 L. Esclapez, P. C. Ma, E. Mayhew, R. Xu, S. Stouffer, T. Lee, H. Wang, and M. Ihme, "Fuel effects on lean blow-out in a realistic gas turbine combustor," *Combust. Flame* **181**, 82–99 (2017).
- 14 F. Rebosio, A. Widenhorn, B. Noll, and M. Aigner, "Numerical simulation of a gas turbine model combustor operated near the lean extinction limit," in *ASME Turbo Expo* (American Society of Mechanical Engineers Digital Collection, 2010) pp. 603–612.
- 15 H. Lu, W. Chen, C. Zou, and H. Yao, "Large-eddy simulation of Sandia Flame F using structural subgrid-scale models and partially-stirred-reactor approach," *Phys. Fluids* **31**, 045109 (2019).
- 16 H. Pitsch, "Improved pollutant predictions in large-eddy simulations of turbulent non-premixed combustion by considering scalar dissipation rate fluctuations," *Proc. Combust. Inst.* **29**, 1971–1978 (2002).
- 17 A. Felden, L. Esclapez, E. Riber, B. Cuenot, and H. Wang, "Including real fuel chemistry in LES of turbulent spray combustion," *Combust. Flame* **193**, 397–416 (2018).
- 18 H. Choi and P. Moin, "Grid-point requirements for large eddy simulation: Chapman's estimates revisited," *Phys. Fluids* **24**, 011702 (2012).
- 19 S. Rezaeiravesh and M. Liefvendahl, "Effect of grid resolution on large eddy simulation of wall-bounded turbulence," *Phys. Fluids* **30**, 055106 (2018).
- 20 X. I. A. Yang and K. P. Griffin, "Grid-point and time-step requirements for direct numerical simulation and large-eddy simulation," *Phys. Fluids* **33**, 015108 (2021).
- 21 G. Boudier, L. Gicquel, and T. Poinso, "Effects of mesh resolution on large eddy simulation of reacting flows in complex geometry combustors," *Combust. Flame* **155**, 196–214 (2008).
- 22 K. M. Almohammadi, D. B. Ingham, L. Ma, and M. Pourkashan, "Computational fluid dynamics (CFD) mesh independency techniques for a straight blade vertical axis wind turbine," *Energy* **58**, 483–493 (2013).
- 23 P.-J. Frey and F. Alauzet, "Anisotropic mesh adaptation for cfd computations," *Comput. Methods in Appl. Mech. Eng.* **194**, 5068–5082 (2005).
- 24 A. Loseille, A. Dervieux, and F. Alauzet, "Fully anisotropic goal-oriented mesh adaptation for 3d steady euler equations," *J. Comput. Phys.* **229**, 2866–2897 (2010).
- 25 C. Hertel and J. Fröhlich, "Error reduction in les via adaptive moving grids," in *Quality and Reliability of Large-Eddy Simulations II* (Springer, 2011) pp. 309–318.
- 26 M. Rai and D. Anderson, "The use of adaptive grids in conjunction with shock capturing methods," in *5th Computational Fluid Dynamics Conference* (1981) p. 1012.
- 27 M. J. Berger and J. Olinger, "Adaptive mesh refinement for hyperbolic partial differential equations," *J. Comput. Phys.* **53**, 484–512 (1984).
- 28 E. Pomraning, K. Richards, and P. Senecal, "Modeling turbulent combustion using a rans model, detailed chemistry, and adaptive mesh refinement," *Tech. Rep.* (SAE Technical Paper, 2014).
- 29 J. Larsson and Q. Wang, "The prospect of using large eddy and detached eddy simulations in engineering design, and the research required to get there," *Philos. T. R. Soc. A.* **372**, 20130329 (2014).
- 30 O. Anteparo, O. Lehmkuhl, R. Borrell, J. Chiva, and A. Oliva, "Parallel adaptive mesh refinement for large-eddy simulations of turbulent flows," *Comput. Fluids* **110**, 48–61 (2015).
- 31 S. Toosi and J. Larsson, "Towards systematic grid selection in les: Identifying the optimal spatial resolution by minimizing the solution sensitivity," *Comput. Fluids* **104488** (2020).
- 32 R. Payri, R. Novella, M. Carreres, and M. Belmar-Gil, "Modeling gaseous non-reactive flow in a lean direct injection gas turbine combustor through an advanced mesh control strategy," *Proc. Inst. Mech., Part G: Journal of Aerospace Engineering* **0954410020919619** (2020).
- 33 S. B. Pope, "Turbulent flows," (2001).
- 34 P. Benard, G. Balarac, V. Moureau, C. Dobrzynski, G. Lartigue, and Y. d'Angelo, "Mesh adaptation for large-eddy simulations in complex geometries," *Int. J. Numer. Methods Fluids* **81**, 719–740 (2016).
- 35 G. Daviller, M. Brebion, P. Xavier, G. Staffelbach, J.-D. Müller, and T. Poinso, "A mesh adaptation strategy to predict pressure losses in les of swirled flows," *Flow Turbul. Combust.* **99**, 93–118 (2017).
- 36 M. Emmett, E. Motheau, W. Zhang, M. Minion, and J. B. Bell, "A fourth-order adaptive mesh refinement algorithm for the multicomponent, reacting compressible navier–stokes equations," *Combust. Theory Model* **23**, 592–625 (2019).
- 37 A. Sjunnesson, C. Nelsson, and E. Max, "LDA Measurements of velocities and turbulence in a bluff body stabilized flame," 4th International Conference on Laser Anemometry - Advances and Application, *ASME* **3**, 83–90 (1991).
- 38 A. Sjunnesson and P. Henrikson, "CARS measurements and visualization of reacting flows in a bluff body stabilized flame," 28th Joint Propulsion Conference and Exhibit, *AIAA* 92-3650 (1992).

- <sup>39</sup>A. Sjunnesson, S. Olovsson, and B. Sjöblom, "Validation Rig-A tool for flame studies," 10th International Symposium on Air Breathing Engines, 385–393 (1991).
- <sup>40</sup>P. A. T. Cocks, M. C. Soteriou, and V. Sankaran, "Impact of numerics on the predictive capabilities of reacting flow LES," *Combust. Flame* **162**, 3394–3411 (2015).
- <sup>41</sup>B. Rochette, F. Collin-Bastiani, L. Gicquel, O. Vermorel, D. Veynante, and T. Poinso, "Influence of chemical schemes, numerical method and dynamic turbulent combustion modeling on LES of premixed turbulent flames," *Combust. Flame* **191**, 417–430 (2018).
- <sup>42</sup>C. Fureby, "Large eddy simulation of turbulent reacting flows with conjugate heat transfer and radiative heat transfer," *Proc. Combust. Inst.* (2020).
- <sup>43</sup>V. Sankaran and T. Gallagher, "Grid convergence in les of bluff body stabilized flames," in *55th AIAA Aerospace Sciences Meeting* (2017) p. 1791.
- <sup>44</sup>S. A. Drennan, G. Kumar, and S. Liu, "Developing grid-convergent LES simulations of augmentor combustion with automatic meshing and adaptive mesh refinement," *AIAA SciTech Forum - 55th AIAA Aerosp. Sci. Meet.* (2017), 10.2514/6.2017-1574.
- <sup>45</sup>W. Meier, P. Weigand, X. Duan, and R. Giezendanner-Thoben, "Detailed characterization of the dynamics of thermoacoustic pulsations in a lean premixed swirl flame," *Combust. Flame* **150**, 2–26 (2007).
- <sup>46</sup>P. Bénard, G. Lartigue, V. Moureau, and R. Mercier, "Large-eddy simulation of the lean-premixed preccinsta burner with wall heat loss," *Proc. Combust. Inst.* **37**, 5233–5243 (2019).
- <sup>47</sup>C. Dapogny, C. Dobrzynski, and P. Frey, "Three-dimensional adaptive domain remeshing, implicit domain meshing, and applications to free and moving boundary problems," *J. Comput. Phys.* **262**, 358–378 (2014).
- <sup>48</sup>S. M. Mitran, "A comparison of adaptive mesh refinement approaches for large eddy simulation," *Tech. Rep.* (Washington Univ Seattle Dept of Applied Mathematics, 2001).
- <sup>49</sup>P. Chassaing, R. Antonia, F. Anselmet, L. Joly, and S. Sarkar, *Variable density fluid turbulence*, Vol. 69 (Springer Science & Business Media, 2002).
- <sup>50</sup>F. Kock and H. Herwig, "Entropy production calculation for turbulent shear flows and their implementation in cfd codes," *Int. J. Heat Fluid Fl.* **26**, 672–680 (2005).
- <sup>51</sup>T. Poinso and S. Lele, "Boundary conditions for direct simulations of compressible viscous flows," *J. Comput. Phys.* **101**, 104–129 (1992).
- <sup>52</sup>P. Sagaut, *Large eddy simulation for incompressible flows: an introduction* (Springer Science & Business Media, 2006).
- <sup>53</sup>O. Zeman, "Dilatation dissipation: the concept and application in modeling compressible mixing layers," *Phys. Fluids A: Fluid Dynamics* **2**, 178–188 (1990).
- <sup>54</sup>H. Pitsch, "Large-Eddy Simulation of Turbulent Combustion," *Annu. Rev. Fluid Mech.* **38**, 453–482 (2005).
- <sup>55</sup>T. Butler and P. O’rourke, "A numerical method for two dimensional unsteady reacting flows," *Symp. Combust. Proc.*, **16**, 1503–1515 (1977).
- <sup>56</sup>O. Colin and M. Rudgyard, "Development of high-order taylor-galerkin schemes for les," *J. Comput. Phys.* **162**, 338–371 (2000).
- <sup>57</sup>F. Charlette, D. Veynante, and C. Meneveau, "A power-law wrinkling model for LES of premixed turbulent combustion: Part I - non-dynamic formulation and initial tests," *Combust. Flame* **131**, 159–180 (2002).
- <sup>58</sup>F. Charlette, C. Meneveau, and D. Veynante, "A Power-Law Flame Wrinkling Model for LES of Premixed Turbulent Combustion Part II: Dynamic Formulation," *Combust. Flame* **197**, 181–197 (2002).
- <sup>59</sup>G. Kuenne, A. Ketelheun, and J. Janicka, "LES modeling of premixed combustion using a thickened flame approach coupled with FGM tabulated chemistry," *Combust. Flame* **158**, 1750–1767 (2011).
- <sup>60</sup>J.-P. L gier, T. Poinso, and D. Veynante, "Dynamically thickened flame LES model for premixed and non-premixed turbulent combustion," in (Center for Turbulence Research, NASA Ames/Stanford Univ., 2000) pp. 157–168.
- <sup>61</sup>It is worth notice that if  $F$  can be described by a Gaussian distribution,  $F_{eff}$  statistically does not underestimate the local maximum thickening  $F$  for the 84.15% of the time, which is considered to be a reasonable condition.
- <sup>62</sup>P. A. T. Cocks, M. C. Soteriou, and V. Sankaran, "Impact of numerics on the predictive capabilities of reacting flow LES," *Combust. Flame* **162**, 3394–3411 (2015).
- <sup>63</sup>A. Ghani, T. Poinso, L. Gicquel, and G. Staffelbach, "LES of longitudinal and transverse self-excited combustion instabilities in a bluff-body stabilized turbulent premixed flame," *Combust. Flame* **162**, 4075–4083 (2015).
- <sup>64</sup>N. Zettervall, K. Nordin-Bates, E. J. K. Nilsson, and C. Fureby, "Large Eddy Simulation of a premixed bluff body stabilized flame using global and skeletal reaction mechanisms," *Combust. Flame*, 1–22 (2017).
- <sup>65</sup>T. Sch nfeld and M. Rudgyard, "Steady and unsteady flows simulations using the hybrid flow solver AVBP," *AIAA J.* **37**, 1378–1385 (1999).
- <sup>66</sup>P. D. Lax and B. Wendroff, "Difference schemes for hyperbolic equations with high order of accuracy," *Commun. Pure Appl. Math.* **17**, 381–398 (1964).
- <sup>67</sup>N. Guezennec and T. Poinso, "Acoustically nonreflecting and reflecting boundary conditions for vorticity injection in compressible solvers," *AIAA J.* **47**, 1709–1722 (2009).
- <sup>68</sup>Note that for all meshes generated in this work, the minimum cell sized is kept the same as the reference mesh in order to obtained a computational cost directly proportional to the number of elements (without modifying the time-step due to CFL condition).
- <sup>69</sup>W. Meier, P. Weigand, X. R. Duan, and R. Giezendanner-Thoben, "Detailed characterization of the dynamics of thermoacoustic pulsations in a lean premixed swirl flame," *Combust. Flame* **150**, 2–26 (2007).
- <sup>70</sup>P. Weigand, X. Duan, W. Meier, U. Meier, M. Aigner, and C. B rat, "Experimental investigations of an oscillating lean premixed ch4/air swirl flame in a gas turbine model combustor," in *European Combustion Meeting* (2005).
- <sup>71</sup>P. Weigand, W. Meier, X. Duan, and M. Aigner, "Laser based investigations of thermo-acoustic instabilities in a lean premixed gas turbine model combustor," in *Turbo Expo: Power for Land, Sea, and Air*, Vol. 42363 (2006) pp. 237–245.
- <sup>72</sup>Z. Yin, P. Nau, and W. Meier, "Responses of combustor surface temperature to flame shape transitions in a turbulent bi-stable swirl flame," *Exp. Therm. Fluid Sci.* **82**, 50–57 (2017).
- <sup>73</sup>B. Franzelli, E. Riber, L. Y. Gicquel, and T. Poinso, "Large Eddy Simulation of combustion instabilities in a lean partially premixed swirled flame," *Combust. Flame* **159**, 621–637 (2012).
- <sup>74</sup>B. Franzelli, E. Riber, and B. Cuenot, "Impact of the chemical description on a Large Eddy Simulation of a lean partially premixed swirled flame," *Comptes Rendus M canique* **341**, 247–256 (2013).
- <sup>75</sup>D. Fredrich, W. P. Jones, and A. J. Marquis, "The stochastic fields method applied to a partially premixed swirl flame with wall heat transfer," *Combust. Flame* **205**, 446–456 (2019).
- <sup>76</sup>J. Galpin, A. Naudin, L. Vervisch, C. Angelberger, O. Colin, and P. Domingo, "Large-eddy simulation of a fuel-lean premixed turbulent swirl-burner," *Combust. Flame* **155**, 247–266 (2008).
- <sup>77</sup>B. Fiorina, R. Vicquelin, P. Auzillon, N. Darabiha, O. Gicquel, and D. Veynante, "A filtered tabulated chemistry model for les of premixed combustion," *Combust. Flame* **157**, 465–475 (2010).
- <sup>78</sup>G. Albuze, T. Poinso, and L. Gicquel, "Chemical kinetics modeling and les combustion model effects on a perfectly premixed burner," *Comptes Rendus M canique* **337**, 318–328 (2009).
- <sup>79</sup>P. S. Volpiani, T. Schmitt, and D. Veynante, "Large eddy simulation of a turbulent swirling premixed flame coupling the TFLES model with a dynamic wrinkling formulation," *Combust. Flame* **180**, 124–135 (2017).
- <sup>80</sup>D. Fredrich, W. P. Jones, and A. J. Marquis, "Thermo-acoustic instabilities in the preccinsta combustor investigated using a compressible les-pdf approach," *Flow Turbul. Combust.*, 1–17 (2020).
- <sup>81</sup>F. Gao and E. E. O’Brien, "A large-eddy simulation scheme for turbulent reacting flows," *Phys. Fluids A Fluid Dyn.* **5**, 1282–1284 (1993).
- <sup>82</sup>D. Laera, P. W. Agostinelli, L. Selle, Q. Caz res, G. Oztarlik, T. Schuller, L. Gicquel, and T. Poinso, "Stabilization mechanisms of CH4 premixed swirled flame enriched with a non-premixed hydrogen injection," *Proc. Combust. Inst.* - in press, (2020), <https://doi.org/10.1016/j.proci.2020.06.378>.
- <sup>83</sup>P. Benard, G. Lartigue, V. Moureau, and R. Mercier, "Large-Eddy Simulation of the lean-premixed PRECCINSTA burner with wall heat loss," *Proc. Combust. Inst.* **37**, 5233–5243 (2019).
- <sup>84</sup>N. Syred, "A review of oscillation mechanisms and the role of the precessing vortex core (pvc) in swirl combustion systems," *Prog Energ Combust* **32**, 93–161 (2006).
- <sup>85</sup>M. St hr, K. Oberleithner, M. Sieber, Z. Yin, and W. Meier, "Experimental Study of Transient Mechanisms of Bistable Flame Shape Transitions in a Swirl Combustor," *J. Eng. Gas Turbines Power* **140** (2018), 10.1115/1.4037724.

- <sup>86</sup>K. Oberleithner, M. Stöhr, S. H. Im, C. M. Arndt, and A. M. Steinberg, "Formation and flame-induced suppression of the precessing vortex core in a swirl combustor: Experiments and linear stability analysis," *Combust. Flame* **162**, 3100–3114 (2015).